

pubs.acs.org/synthbio Research Article

# Parameterized Computational Framework for the Description and Design of Genetic Circuits of Morphogenesis Based on Contact-Dependent Signaling and Changes in Cell—Cell Adhesion

Calvin Lam,\*,○ Sajeev Saluja,○ George Courcoubetis,○ Dottie Yu, Christian Chung, Josquin Courte, and Leonardo Morsut\*



Cite This: ACS Synth. Biol. 2022, 11, 1417-1439



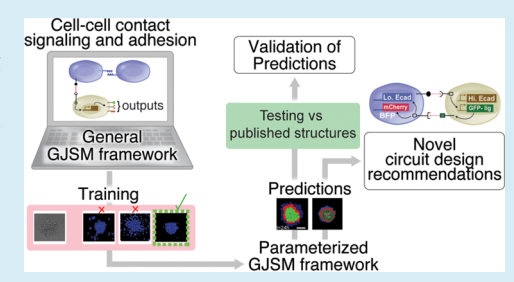
ACCESS I

III Metrics & More

Article Recommendations

Supporting Information

**ABSTRACT:** Synthetic development is a nascent field of research that uses the tools of synthetic biology to design genetic programs directing cellular patterning and morphogenesis in higher eukaryotic cells, such as mammalian cells. One specific example of such synthetic genetic programs was based on cell—cell contact-dependent signaling using synthetic Notch pathways and was shown to drive the formation of multilayered spheroids by modulating cell—cell adhesion *via* differential expression of cadherin family proteins in a mouse fibroblast cell line (L929). The design method for these genetic programs relied on trial and error, which limited the number of possible circuits and parameter ranges that could be explored. Here, we build a parameterized computational framework that, given a



cell—cell communication network driving changes in cell adhesion and initial conditions as inputs, predicts developmental trajectories. We first built a general computational framework where contact-dependent cell—cell signaling networks and changes in cell—cell adhesion could be designed in a modular fashion. We then used a set of available *in vitro* results (that we call the "training set" in analogy to similar pipelines in the machine learning field) to parameterize the computational model with values for adhesion and signaling. We then show that this parameterized model can qualitatively predict experimental results from a "testing set" of available *in vitro* data that varied the genetic network in terms of adhesion combinations, initial number of cells, and even changes to the network architecture. Finally, this parameterized model is used to recommend novel network implementation for the formation of a four-layered structure that has not been reported previously. The framework that we develop here could function as a testing ground to identify the reachable space of morphologies that can be obtained by controlling contact-dependent cell—cell communications and adhesion with these molecular tools and in this cellular system. Additionally, we discuss how the model could be expanded to include other forms of communication or effectors for the computational design of the next generation of synthetic developmental trajectories.

**KEYWORDS:** synthetic biology, self-organization, tissue engineering, computational modeling, cellular Potts, juxtacrine signaling, synNotch, patterning, morphogenesis

# **■ INTRODUCTION**

Multicellular mammalian systems display a remarkable capacity for self-organization into a myriad of different shapes and forms, from branching lung epithelia to elongating tail bud mesenchyme. These phenomena of self-organization in mammalian morphogenetic systems are not yet completely understood and are being investigated intensively, *e.g.*, *via* analysis, perturbation, and modeling of model organisms. <sup>1-9</sup> From these studies, several factors that seem to be important for self-organization are being recognized, among them are chemical, epigenetic, bioelectrical, morphogen, mechanical, and cell—cell communication signals. <sup>10–12</sup> The identification and characterization of these factors will ultimately allow implementation in simplified "toy models" (*i.e.*, minimal models akin to the pendulum for physics <sup>13</sup>) of synthetic development both *in silico* and *in vitro*. <sup>13–20</sup>

One paradigmatic example of morphogenetic systems is the mechanochemical systems, which are composed of cell—cell signaling and changes in cellular or tissue mechanics. These systems have been shown to be at play in a number of natural systems, <sup>21,22</sup> and computational models have been developed to capture both signaling and mechanical changes in integrated models. <sup>23</sup>

Among mechanical effectors, cell-cell adhesion has been recognized as an important effector of multicellular morpho-

Received: July 10, 2020 Published: April 1, 2022





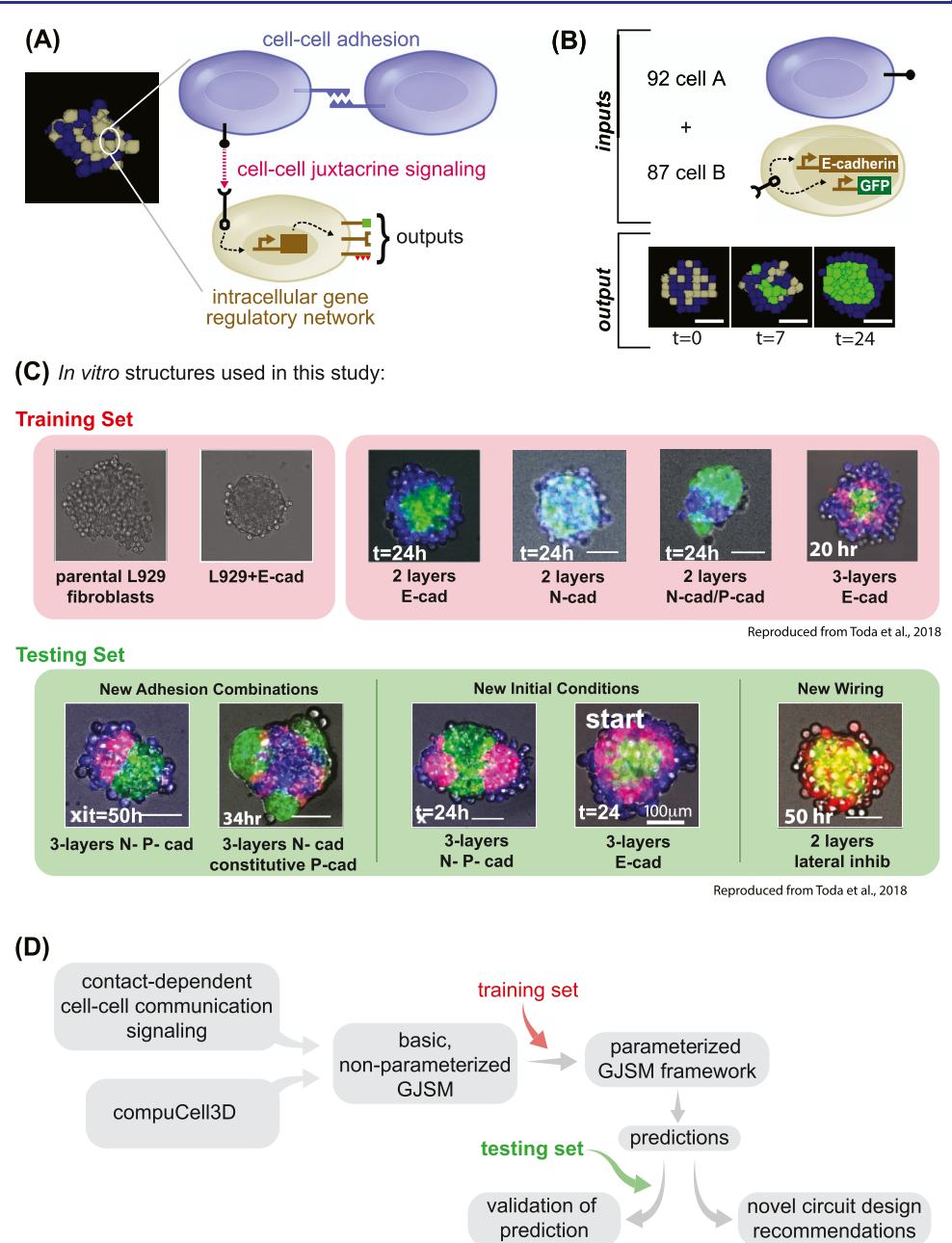


Figure 1. Model is developed and tested via a training set/testing set approach to parameterize and test generalization capacity. (A) Example of a snapshot of the computational model output on the left; highlighted on the right is the schematic of the logic that drives the cell dynamics: cell-cell adhesion and cell-cell juxtacrine signaling combined together. Cells can communicate to one another if, as in this case of the blue type and gray type, they have the cognate signal and receptor. Outputs of the communication can be a change in fate, which can signify: new ligand production or changes in cell adhesion. (B) We define input to our computational model as the initial conditions of how many cells of the different types there are and the "genotype" of cells of the different types; the output is a simulation of the developmental trajectory. (C) Snapshot of the in vitro structures used in this study to build the computational model. The red background highlights the structures used for the training set; the green background highlights the structures for the testing set. For each structure, a microscopic image of L929 cells engineered with different networks is shown, as described later in the text, and imaged at the indicated time point. The two-layer indicates a network of signaling where  $A \rightarrow B$ , and the three-layer one is where  $A \rightarrow B \rightarrow A$  (see later for more details). Adhesion molecules are as follows: E-cad, E-cadherin; N-cad, N-cadherin; P-cad, P-cadherin. Scale bar is 17.5 pixels in silico, 100 µm in vitro. (D) Conceptual diagram of the flow we followed in the entire paper: each box represents a conceptual item that we used and combined logically. First, we generate a basic generalized juxtacrine signaling model (GJSM) by combining CompuCell3D with custom code for cell-cell contact-dependent signaling and change in cell types; then, we use the training set to identify parameters capable of recapitulating in vitro training set behaviors; finally, we use that model to make prediction, which is tested by comparing it with the testing set or used to make recommendations for novel synthetic genomes. Microscopic images with a gray background are reproduced from Toda, S.; Blauch, L. R.; Tang, S. K. Y.; Morsut, L.; Lim, W. A. Programming Self-Organizing Multicellular Structures with Synthetic Cell-Cell Signaling. Science 2018, 361 (6398), 156-162. Copyright 2018 AAAS. Reprinted with permission from AAAS.

genesis. In its simplest form, differential adhesion between cells can favor cell rearrangements that bring cells with high cell—

cell adhesion closer together. This "differential adhesion" hypothesis has been studied in cellular systems where adhesion

levels were changed via constitutive adhesion protein over-expression<sup>24</sup> and also via computational systems where adhesion levels can be decided by the user (including CompuCell3D<sup>25</sup>).

Contact-dependent cell-cell communication networks have also been recognized as powerful sources for multicellular patterning in vivo, 26-29 and computational models have been developed and used to show the patterning potential of contact-dependent networks. Recently, synthetic variants of cell-cell contact-dependent signaling have been developed and named synthetic Notch or synNotch. SynNotch is based on the native Notch receptor, which relies on contactdependent, or juxtacrine, signaling. 32 SynNotch has been engineered such that it can respond to synthetic ligands, such as green fluorescence protein (GFP), with user-defined outputs. If a cell expressing GFP-ligand (sender cell) is in contact with a cell expressing anti-GFP receptor (receiver cell), then the receiver cell will start to produce user-defined target genes. SynNotch pathways allow the user to define the input and the output of communication channels that are orthogonal to endogenous signaling. This synthetic cell-cell contact signaling system alone has been used to drive patterning in two-dimensional (2D) in epithelial cells.<sup>33</sup>

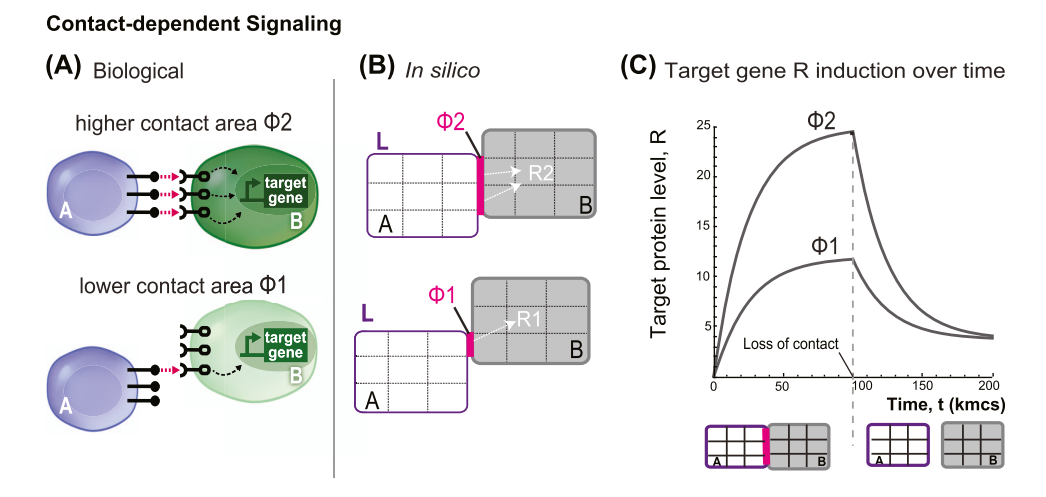
A first example of a synthetic artificial genetic network for mechanochemical-driven morphogenesis was recently described by combining cell-cell adhesion and cell-cell contact-mediated communication by Toda et al. 19 In this system, artificial genetic networks intertwine two morphogenetic factors: cell-cell contact-dependent signaling and concomitant changes in cell-cell adhesion. Changes of cellcell adhesion are initiated via synNotch cell-cell communication pathways, leading to dynamic and localized changes in cell-cell adhesion strengths. With these networks, mouse fibroblast cells can be designed such that they follow userdefined morphogenetic trajectories to generate multilayered spheroids starting from a random mixture of one or two genetically different cell types. That work demonstrated that simple networks of cell-cell communications with changes in cell adhesion can drive developmental trajectories that have features commonly found in developing morphogenetic

One limitation of synthetic development studies lies in the design phase that relies heavily on lengthy trial-and-error iterations. As the range of parameters and designs that can be tested is limited to scientists' best guesses, a systematic analysis of design space is not possible and interesting solutions may be overlooked. In other areas of synthetic biology, this initial phase of intuitive design has been followed by a phase of computational systems development. These computational systems are used initially for the description and then the design of the systems in a way that can lead to implementation. <sup>34–36</sup> One remarkable example is the decadelong development of Cello, a computational framework for the design and implementation of bacterial unicellular gene regulatory networks.<sup>37</sup> In Cello, users can give design specifications in silico of combinatorial logic, and the computational system converts them into complete DNA sequences encoding transcriptional logic circuits that can be executed in bacterial cells. Similar efforts in mammalian cells are occurring with a lag, beginning with intracellular circuits.<sup>38</sup> Computational efforts for helping the design of user-defined structures in multicellular systems have been initiated, e.g., the design of structure obtained by sculpting of muscle and

epithelial cells in "xenobots" or the design of culture and initial conditions for aggregates of human stem cells to control their organization. Until recently, no example of a computational system for description at the level of genetic circuits of morphogenesis was available for assisting with design. The *in vitro* system in Toda seems perfectly placed to provide a case study as it has all of the features of a minimal "toy model" of synthetic circuit-guided morphogenesis (and it has attracted efforts from other groups as well 42,43): it uses mammalian cells (mouse fibroblast line L929), it has logically minimal circuits, shows the genotype-to-phenotype relationships, and has explored the phenotypic consequences of changes in either cell—cell adhesion and/or network topologies.

Here, we describe how we have built a computational framework for the description and design of genetic circuits of morphogenesis based on contact-dependent signaling and changes in cell-cell adhesion. This computational system can take, as input, an artificial genetic circuit of cell-cell communication, changes in cell adhesion (a "synthetic genome") and initial conditions (e.g., number of cells of each type), and produce, as output, the developmental trajectory (Figure 1A,B). The computational system is based on a stochastic cellular Potts environment implemented in CompuCell3D, which allows the simulation of adhesionbased rearrangements, cell movement, and cell division.<sup>25</sup> We overlaid a custom code to model cell-cell contact-dependent signaling by defining cell types and encoding information about cell-cell contact. We then proceed to parameterize the system with specific parameter values that model the cellular type at hand (mouse fibroblast line L929), the communication system (synNotch-based contact-dependent signaling), and the morphogenetic effectors (adhesion molecules). To do so, we split the available in vitro data set into a "training set" and a "testing set" (Figure 1C), following a framework for model identification common in machine learning. We use the "training set" to identify parameters for the *in silico* model. The synthetic genomes of the training set are chosen such that they would contain all of the basic primitives of signaling and adhesion interactions that are found in the in vitro implementations: adhesion strengths, cell movement and proliferation, and signaling. Subsequently, we use the testing set to test if the parameterization can capture features of the systems outside those used for parameterization. Finally, we identify a synthetic genome in silico that can generate novel four-layer structures (not present in the in vitro data set) and provide a recommendation for the synthetic genome that could implement it in vitro in the mouse fibroblast cell line L929, with a combination of available parts (Figure 1D). Figures 2-4 describe the model parameterization based on in vitro data. Figures 5-8 show examples of the capacity of the parameterized computational system to quantitatively reproduce emergent properties not used in parameterization (Figure 5) and qualitatively predict developmental trajectories from the testing set that have different adhesion (Figure 6), different initial number of cells (Figure 7), or changes to the genetic network (Figure 8). Figure 9 shows the recommendation for the synthetic genome for the four-layered structure in vitro with a combination of available parts.

This example of the development of a computational pipeline is among the first examples of computational systems developed and used for the description and design of genetic circuits for synthetic morphogenesis based on synNotch and changes in adhesion in mouse fibroblast cells. We think it



#### Contact-dependent Changes in Cell State

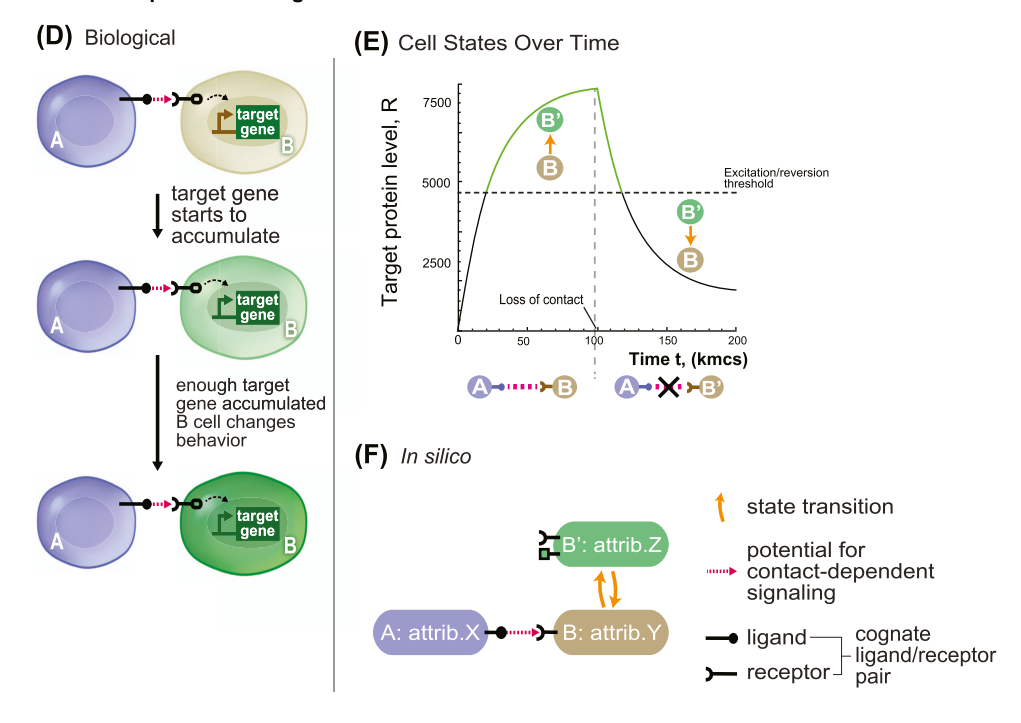


Figure 2. Concepts underlying the computational model (see the Methods section for details and generalized model). Schematic description of the computational model for contact-dependent cell state changes in cell aggregates. (A) Representation of the biological communication between cell pairs A and B. A cells express ligand (black circle + stick) and B cells express receptor (black). With contact (pink arrow), B cells receive signal (dashed arrow) that triggers the expression of the target gene (green). In the cells below, the amount of contact surface is lower; hence, the signaling (dashed arrow) toward the target gene is less intense. (B) The in silico model shows a simplified representation of the cell-cell signaling process with parameters: ligand amount (L, purple), surface area of contact (Φ, pink), and net signal (white arrow to target gene R). Cells (A) are the sender in the communication, and cells B are the receiver. In this schematic, in silico cells are objects of nine pixels. The cell pair at the top has a higher level of signaling compared to the upper pair due to a larger surface area of contact ( $\Phi 2 > \Phi 1$ , 2 pixels compared to 1). (C) Time evolution of the target gene level in the receiving cell B; cells A and B are placed in contact at time zero and kept in the same configuration for 100,000 steps of simulation and then moved far apart to stop signaling. Target gene levels are followed over time for two different values of shared surface area  $\Phi$ , with  $\Phi 2 > \Phi 1$ , with all other parameters kept identical. (D-F) Model representation of the cell behavior state change. (D) Representation of the biological "effector gene" activation: a sender cell A (blue) activates a receiver cell B (gray) to induce a target gene (green) that encodes for an effector protein. Over time, cell B accumulates target gene products, and at a certain threshold, the effector gene product causes cell behavior to change (e.g., stronger adhesion to neighbors) such that the cell transitions from type B to B'. (E) The graph shows the progression of target gene level over time for a B cell that is initially in contact with an A cell and is then isolated at 100,000 steps. The threshold for the excited state is shown as the dotted horizontal line. At the start, the B cell is in the basal state (black solid line), but when the target gene level passes the excited-state threshold, B cell becomes a B' cell. The B' cell remains in the active state (green solid line) until target gene levels drop below the activation threshold and reverts to B (line goes back to solid black). (F) In silico representation of the state transition and communication relationship between cells A, B, and B'. Orange curved arrows indicate state transitions. Matching ligand/receptor pairs indicate a communication channel from A to B that promotes the state change of B to B'.

represents an example that can be built upon in the future in the field either expanding the analysis of the reachable structures with these parts or by extending it with other parts. The description here of how we went about the computational system parameterization with the available parts (synNotch signaling and cadherin-based adhesion in L929 cells) could serve as a template for the expansion to other cell types, signaling currencies and morphogenetic effectors (e.g., soluble ligand-based, bioelectricity, cytoskeletal, etc.). We think that our work provides a first necessary step toward the development of complete pipelines with computational design and in vitro implementation of synthetic developmental trajectories in multicellular systems.

## RESULTS

Framework for Modeling of Cell–Cell Contact Signaling and Cell State Changes in CompuCell3D (Complete Details in the Methods Section). We first built a computational framework that could simulate the development of multicellular spheroids informed by a "synthetic genome" that controls their cell—cell communication, adhesion, and movement. The CompuCell3D platform can simulate adhesion, movement, division, and presence of different cell "types"; we added a new code for contact-dependent signaling-mediated change of cell type.

Briefly, in CompuCell3D,  $^{25}$  each cell  $\sigma(i)$  is defined as comprising a user-defined number of atomic pixels, whose position in space can change over time with a stochastic algorithm. The probability that a pixel will move is calculated by CompuCell3D for each attempt of movement at each time interval (known as Monte Carlo step (mcs)) with the following equation

$$P = E^{-\Delta H/T} \tag{1}$$

where  $\Delta H$  is the difference in "entropy energy" between the configurations before the change versus after the change, and T is a "temperature" parameter of the cell that is attempting the change, which can be interpreted as cell motility. Governed by this equation, a system will dynamically change configuration over time toward configurations that minimize entropy energy (H). Entropy energy for a given configuration of cells is calculated based on cell—cell contact and cell shape as follows

$$H = \sum_{i,j} J_{\sigma(i),\sigma(j)} (1 - \delta_{\sigma(i),\sigma(j)})$$

$$+ + \sum_{\sigma} (\lambda(\sigma)(\operatorname{Sur}(\sigma) - \operatorname{Sur}_{\operatorname{Tar}}(\sigma))^{2}$$

$$+ \lambda(\sigma)(\operatorname{Vol}(\sigma) - \operatorname{Vol}_{\operatorname{Tar}}(\sigma))^{2})$$
(2)

The first term of this equation deals with how cell—cell contacts contribute to H. Whether two cells are in contact is encoded in a Kronecker delta  $\delta_{\sigma(i),\sigma(j)}$  that is 0 if cells i and j are neighbors and 1 otherwise and can be thought of as an adjacency matrix. If two cells are in contact, they will contribute proportionally to H the number of pixels that are in contact-weighted by the adhesion matrix J. The adhesion matrix  $J_{\sigma(i),\sigma(j)}$  defines an adhesion weight between cells i and j. Higher adhesion values in the adhesion matrix correspond to increased entropy, less "stable" conformations, and hence a lower likelihood that neighboring cells will remain close. Consequently, higher adhesion values in the model correspond to a lower likelihood of cells sticking together and can

therefore be interpreted as corresponding to lower adhesion strength.

The second line of eq 2 deals with how cell shape contributes to H. Cell shape contributions are defined as the sum of all deviations of the current volume of each cell from target volume (Vol<sub>Tar</sub>) and surface (Sur<sub>Tar</sub>), weighted with a "deformability" parameter  $\lambda$ . As cells deform and stray further from their target volume or surface, entropy energy (H) increases. The amount that the deformation is penalized is weighted via  $\lambda$ , with lower values of  $\lambda$  allowing larger deformations.

In this context, cell types can be defined as subsets of the total set of cells that share certain features (*e.g.*, adhesion, motility, deformability, or other). Upon cell division, daughter cells inherit the features of the parent cell. One special "cell-type" indication is given to the medium, such that cell-medium adhesion parameters can be defined.

In this framework, we introduced the capacity for cells to be able to influence the behavior of their neighbors, so that a contact-dependent cell-cell communication system could be implemented. The abstract features of the synNotch communications that we want to capture are (i) signaling that is proportional to the amount of shared cell-cell contact surface between the sender and receiver cells that express cognate ligand/receptor pairs, (ii) signaling that is capable of affecting changes in protein production, (iii) that when protein production increases sufficiently, the receiver cell can change from a basal to an activated state, and (iv) that the activated cell can acquire new behaviors such as altered adhesiveness or the capacity to send a new signal (Figure 2A,D). To model these synNotch communications, we conceptually separated the modeling into two parts: signaling-dependent continuous changes in target protein production in receiver cells (Figure 2B,C) and protein-dependent discrete changes in cell behavior (Figure 2E,F). The two parts of the model, continuous signaling and discrete response, are highly modular and can be designed and tested independently of one another.

For modeling contact surface-dependent, continuous changes in target protein production, we introduce a new feature of *in silico* cells, their repertoire of ligands and receptors. Each cell  $\sigma(i)$  can be equipped with ligand\_A through \_Z and with receptor\_A through \_Z. If a cell is equipped with receptor\_X, it can start to accumulate target protein production points if it is in contact with a cell that is expressing the cognate ligand\_X. Cell contact information is encoded in the adjacency matrix (see above), and the response is calculated *via* differential equations to model input-dependent response as follows

$$\frac{\mathrm{d}R}{\mathrm{d}t} = \frac{1}{1 + \mathrm{e}^{-((S-\beta)/\varepsilon)}} - \frac{R}{\kappa} \tag{3.1}$$

here, R is the response (target protein production); S is the signal or input coming from neighbors;  $\beta$  is a constant that controls signaling delay;  $\varepsilon$  is a constant that affects the strength, steepness, and overall geometry of this differential equation; and  $\kappa$  is the degradation constant. Signal (S) can depend on several factors: the number of sender cells contacting the receiver cell, the number of ligands on each sender cell, the number of receptors on the receiver cell, and the amount of contact between sender(s) and receiver. In a simplified two-cell case with sender cell s and receiver cell s, if the receptors on s are in excess, signaling depends primarily on the amount of ligand on cell s and the fraction of s surface

contacting B. If we define L as the number of ligands on cell A's surface and  $\Phi$  as the fraction of A's surface in contact with B's surface, we can then define the signal (S) that cell B receives as  $S = \Phi \times L$  (Figure 2B)

$$\frac{\mathrm{d}R}{\mathrm{d}t} = \frac{1}{1 + \mathrm{e}^{-(((\Phi \times L) - \beta)/\varepsilon)}} - \frac{R}{\kappa}$$
(3.2)

The target protein production for each cell is calculated by numerically solving (eq 3.2) via the forward Euler method. With these definitions, we have cellular signaling that depends on the amount of contacted ligand and obtain a stronger response as the fraction of the shared surface or ligand produced per unit area is increased, as in the case of synNotch signaling 35,44 (Figure 2C). This part of the model accounts for the continuous changes in protein production in receiver cells. For a more detailed explanation, please see the CompuCell3D and the Cellular Potts Formalism and the Generalized Juxtacrine Signaling Model (GJSM) sections.

To model target protein-dependent change in cell behavior, we define thresholds of protein production that induce transition from a basal cell state to an activated state and vice versa. In the example above, if receiver cell B receives sufficient signal to produce a level of protein passing the activation threshold, the cell will become activated, denoted as B' (Figure 2E). Thresholds for state transitions from basal to active and from active to basal can be different, in general, but in the current work, they are kept at the same value. The statemachine schematic for this type of network is shown in Figure 2F. The features of an activated cell's adhesion and signaling can be different from its basal state. For example, B' cells can be more adhesive than B cells to other B' cells. In this way, behavioral transitions are linked to the protein production changes via a threshold, which captures the discrete change in cell behavior observed in cell biology and used in other modeling efforts. 3,4,45 Additionally, or alternatively, cell B' can also gain a communication capacity that was absent in cell B, e.g., the capacity to produce a synthetic ligand for communication. The model itself is general, and any features of B' cells can be different compared to those of B cells, e.g., proliferation, motility, division rate, etc. We note here that the cellular protein production and interactions are chosen to model contact-dependent signaling (also known as juxtacrine). Other signaling mechanisms, such as diffusion-mediated patterning, can be implemented by choosing the appropriate differential equations.

Within this framework, cell rearrangements are nonlinearly dependent on cell—cell signaling networks, adhesion preferences of the cells in the different states, and initial conditions. The number and amount of cell—cell contacts in fact change over time as the systems restructure toward a stable configuration, which depends on the pattern of cell adhesion preferences, but the stability of a given configuration also changes when the cell—cell adhesion properties of the cells change over time as a consequence of cell—cell signaling. This gives rise to a nonlinear system that cannot be treated completely analytically.

**Parameterization of the Model.** With the computational system at hand, we wanted to see if we could parameterize it such that it could describe mouse fibroblast cell line L929 engineered with the synthetic morphogenetic networks based on synNotch and changes in cell adhesion described in ref 19. As detailed below, we first made decisions on basic parameters such as cell size and adhesion range with *in vitro* data from

L929 cells, biological considerations, and feasibility constraints in execution time, and then the rest of the more specific parameters were tuned by parameter scans and comparison with in vitro L929 cells. In this way, we identified a coherent ensemble of parameters that faithfully reproduce in vitro results. We note here that several different sets of numerical values for the parameters could give rise to the same cellular structures in CompuCell3D. For example, we chose 52 as cellmedium adhesion, which restricts the value of adhesion for more adherent cells in the 0-51 range; if we picked a different value for cell-medium adhesion, the precise numerical value for the adhesion of the different adhesion molecule would be different. Further details on the algorithm and parameters can be found in the Methods, In Silico L929 (ISL929) Cell Line Properties, and CompuCell3D and the Cellular Potts Formalism sections, and full lists of simulation parameters can be found in Table S1 for signaling and simulation and Table S2 for adhesion.

Baseline Adhesion, Cell Size, Deformability, and Motility. Cells in the *in vitro* reference experiment are L929 murine fibroblasts; to create an *in silico* version, ISL929, we needed to identify a parameter set that would produce biologically plausible cellular structures. The parameters that needed to be identified are highlighted in yellow in the CompuCell3D equations

$$H = \sum_{i,j} \underline{J_{\sigma(i),\sigma(j)}} (1 - \delta_{\sigma(i),\sigma(j)}) + \sum_{\sigma} (\frac{\lambda}{\sigma})(Sur(\sigma) - \frac{Sur_{Tar}}{\sigma}(\sigma))^{2} + \frac{\lambda}{\sigma}(\sigma)(Vol(\sigma) - \frac{Vol_{Tar}}{\sigma}(\sigma))^{2})$$

For the parameters for cell size and cell shape, we first chose the target surface ( $Sur_{Tar}$ ) and volume ( $Vol_{Tar}$ ) of the cell to correspond to that of a sphere, as the cells are spherical before aggregating *in vitro*. If a cell is too small, then its movement is very volatile due to the small number of pixels that constitute it. On the other hand, a very large cell is slow and requires many Monte Carlo steps (mcs) to move, making it computationally demanding. With this motivation in mind, we set the cells to have a preferred radius of 3 pixels, corresponding to the target volume and surface ( $Vol_{Tar}$  and  $Sur_{Tar}$ ) of 113 pixels. Furthermore, we set the basal energy cost of deforming away from the target volume and area to be  $\lambda$  = 2.2.

With these fixed parameter choices, we moved to identify parameters for temperature (T), which can be interpreted as a motility parameter 25,46 and basal cell-cell and cell-medium adhesion via parameter screening. These parameters are crucial to define a multicellular system's basal "mixability", i.e., capacity of cells to rearrange in a spheroid. To parameterize T and baseline cell-cell and cell-medium adhesion, we first picked an arbitrary value for cell-medium adhesion of 52. The parameter choice for cell-medium adhesion sets the scale for the remaining model parameters, as cells that are not in contact with other cells are always in contact with the medium, and they, e.g., favor cell-cell only if the cell-cell adhesion is lower than the cell-medium. In this system, adhesion between cells contributes positively to the effective energy and, since the stochastic dynamics favor pixel rearrangements that lower the effective energy, higher adhesion magnitudes correspond to a lower adhesion strength.

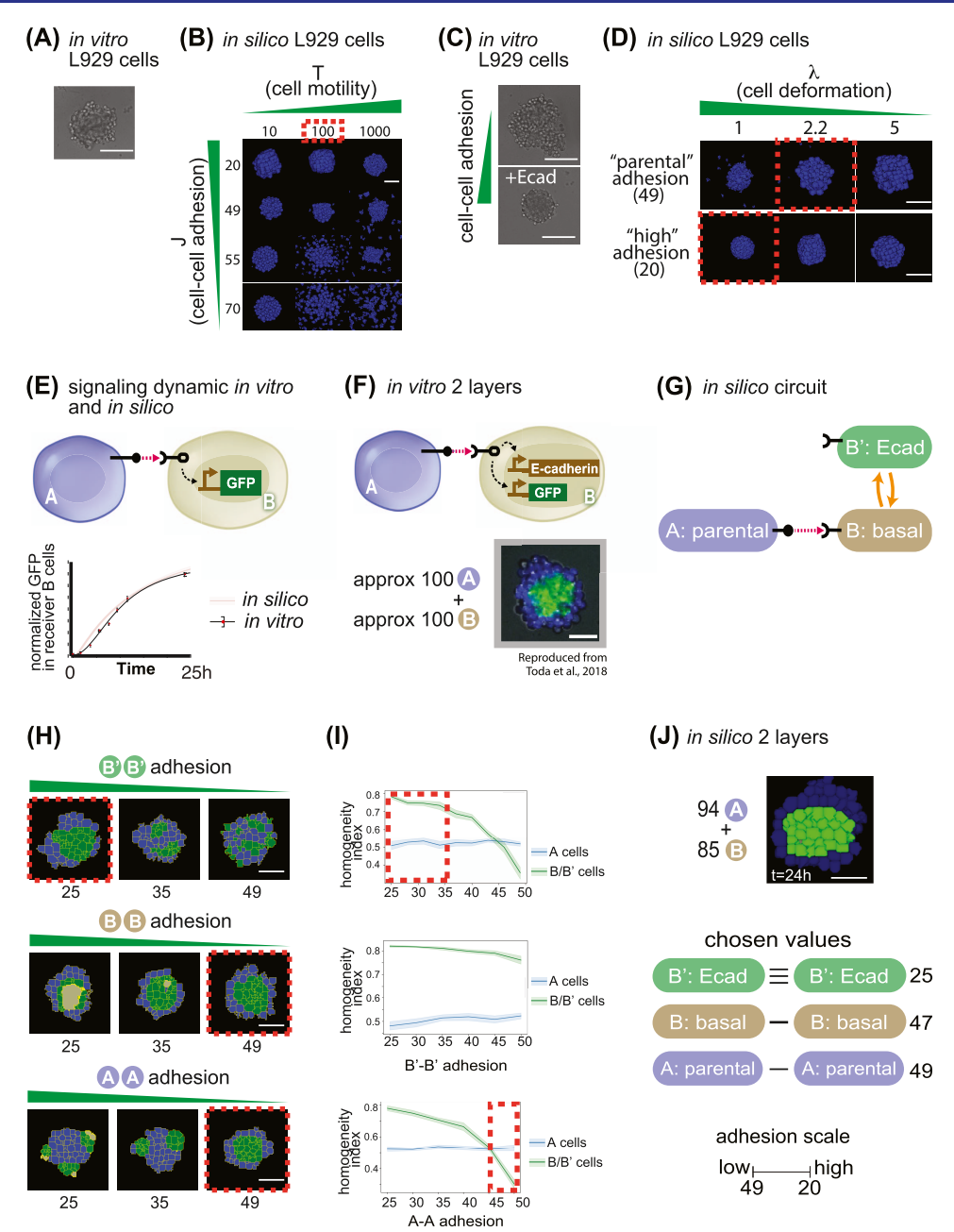


Figure 3. Model parameterization of signaling and adhesion in A → B networks. (A) In vitro picture of 100 parental L929 cells grown for 24 h in a nonadhesive U-bottom well of a 96-well plate. (B) In silico pictures of 100 identical cells grown in a nonadhesive virtual medium for 24 h; as indicated, cells in different snapshots have different parameters for cell movement (x axis) and cell-cell adhesion (y axis). (C) In vitro picture of 100 L929 cells grown for 24 h in a nonadhesive U-bottom well of a 96-well plate, either parental (upper picture) or genetically engineered to overexpress E-cadherin (lower picture). (D) In silico pictures of 100 identical cells grown in a nonadhesive virtual medium for 24 h; as indicated, cells in different snapshots have different parameters for cell deformation (x axis) and cell-cell adhesion (y axis). (E) Diagram of sender A cells and receiver B cells that induce GFP downstream of activation of a contact-dependent receptor (left). Below, the graph of target gene expression over time for B cells for either in silico simulations (red line + shadow standard deviation) or in vitro experiments (black line). (F) Diagram of sender A cells and receiver B cells that induce GFP and E-cadherin downstream of activation of a contact-dependent receptor (top). On the bottom is a result of an in vitro experiment after 24 h of cultivating approximately 100 A cells with 100 B cells. (G) Depiction of the transition network between cell states that is implemented in (F). (H) Starting from 100 A and 100 B cells where the B'-B' adhesions were changed (first line) or the A-A (second line) or the B-B (third line). Red dotted lines indicate the structure that most closely resembles the in vitro implementation (F). (I) Sorting index quantification of a 24 h time point of cells A (blue line) or B (green line) for a range of B'-B' adhesion (first line), A-A adhesions (second line), and B-B adhesions (third line). Red dotted lines represent ranges of behavior that recapitulate in vitro observations. (J) In silico output of input 94 A cells and 85 B cells with the same network as in (H) and with the values for adhesion indicated on the right. Scale bar is 17.5 pixels in silico, 100 µm in vitro. Microscopic images with a gray background are reproduced from Toda, S.; Blauch, L. R.; Tang, S. K. Y.; Morsut, L.; Lim, W. A. Programming Self-Organizing Multicellular Structures with Synthetic Cell-Cell Signaling. Science 2018, 361 (6398), 156-162. Copyright 2018 AAAS. Reprinted with permission from AAAS.

Then, we compared the behavior of an aggregate of 100 L929 cells in vitro with a similar aggregate of ISL929 cells in silico where parameter values of T and cell-cell adhesion were varied within a specified range (Figure 3A,B). As visible from Figure 3A, wild-type L929 cells weakly aggregate to a pseudospherical structure with "rough" edges, biologically indicative of weak cell-cell adhesion. In silico, a range of motility between 10 and 1000 and of cell-cell adhesion between 20 and 70 were tested. As shown in Figure 3B, within 10,000 simulation steps (mcs), T = 10 does not allow cells to move for any of the adhesion parameters. When T = 1000, spheroid formation occurred only for cell-cell adhesion values of 20, whereas higher values for cell-cell adhesion (corresponding to lower adhesion strength) resulted in cells disintegrating from the spheroid, which is not observed in vitro. Moreover, with T = 1000, cell shape was extremely distorted. At T = 100, we obtained a spheroid with rough edges for cell-cell adhesion stronger than cell-medium (49 for cell-cell adhesion vs 52 of cell-medium adhesion-reminder that these values are inversely proportional to the strength of adhesion), similar to the in vitro phenotypes. These observations prompted us to use values of T = 100 for basic temperature, 52 for cell-medium adhesion, and 49 for cell-cell adhesion of cells. These values were used throughout the rest of the simulations presented in this paper.

When performing the adhesion parameter scan, we noticed that lower cell-cell adhesion values (higher adhesion strengths) resulted in larger aggregates, which was not consistent with previous observations in vitro that higher cell-cell adhesion results in more compact aggregates. To further investigate this, we cultivated aggregates of 100 L929 parental cells in U-bottom wells and compared their dimension to aggregates made of 100 L929 cells overexpressing Ecadherin protein, which leads to increased cell-cell adhesion strengths. We observed that the E-cadherin aggregates were indeed smaller than the parental ones in vitro (Figure 3C). To recapitulate this behavior in silico, we conducted a parameter scan of the deformability parameter lambda over two adhesion values. As visible from Figure 3D, a  $\lambda$  = 5 does not allow cells to change shape at all, while  $\lambda = 1$  allows more highly adhesive cells (below 40) to form a compacted spheroid. When set at a value of 2.2, cells with adhesion above 40 formed larger aggregates, as seen in vitro. Based on this analysis, we chose to keep  $\lambda$  at 2.2 for parental cells, but to lower it to 1 for cells with adhesion below 40, such that they would mimic in vitro behavior and form smaller aggregates.

synNotch Signaling for "Two-Layer" Networks. To identify numerical values for the signaling eq 3.1, we use experimental data from a simple in vitro experiment presented in ref 19. A population of receiver cells engineered with the synNotch receptor that activates a GFP target protein were set in contact with a population of sender cells expressing a cognate ligand. Then, fluorescent protein production is tracked over time (Figure 3E). The time dependence of the normalized fluorescence provides the time scale of contact-dependent signaling. To mimic the signal induction dynamics in receiver cells in silico, a simulation was set up to track normalized protein production over time. Equal amounts of sender A and receiver B cells were seeded in two box-shaped sheets, with uniform contact between the two types. Levels of reporter gene in receivers were tracked over time for a total of 24,000 mcs. The signaling parameters  $\beta$ ,  $\kappa$ ,  $\varepsilon$  were heuristically adjusted (not shown) such that the simulation matched the

experimental normalized fluorescence (shown in Figure 3E) (numerical values for  $\beta$ ,  $\kappa$ , and  $\varepsilon$  can be found in Table S1). These parameters capture dynamics specific to synNotch signaling in L929 cells, and we used them as our baseline for all subsequent signaling interactions. Given the temporal dimension of the *in vitro* results, this also gave us a temporal translation between simulation time and real time of 1000 mcs = 1 h.

Adhesion in Two-Layer Networks. We then moved to identify numerical values for the adhesion weights (matrix *J*) of different adhesion molecules. In the in vitro experiments, different levels of E-cadherin (E-cad), N-cadherin (N-cad), and P-cadherin (P-cad) are used to modulate cell-cell adhesion. We first developed an initial relative hierarchy of adhesion strength based on available studies in the literature that pointed to differences in adhesion strength produced between cells expressing different adhesion molecules or even different amounts of the same adhesion molecule.<sup>24</sup> In particular, E-cad, N-cad, and P-cad are preferentially homotypical, but E-cad is stronger and more promiscuous toward N- and P-cad, whereas P- and N-cad are weaker and more selectively homotypical.<sup>47</sup> From this, we generated an adhesion hierarchy where, at similar levels of expression, E-cad produces greater adhesion strength between cells than either N- or P-cad; heterotypic E-cad:P-cad and E-cad:N-cad pairings are more favored than the N-cad:P-cad, and for any given cadherin molecule, low levels of expression produce less adhesion strength than higher levels of expression. With this general hierarchy of the relative strengths of different adhesion pairs, we performed the following parameter screens to identify specific numerical values for adhesion strength parameters.

We started with identifying parameters for E-cad. To do so, we used experimental data from a training set structure that we call "two-layer network": here, sender A cells activate receiver B cells to generate B' cells that produce E-cad adhesion molecule. We knew from the in vitro data that if we started with 100 A cells and 100 B cells randomly mixed, in 24 h, we would obtain a two-layered spheroid with activated B' cells in the innermost layer and A cells on the outside (Figure 3F). In silico, we set up a simulation to mirror the in vitro experiment (Figure 3G). Approximately 100 A cells expressing ligand A were mixed with 100 B cells expressing receptor A; when B cells acquire target protein units above the activation threshold (set at 5263), they convert to B' (Figure 3H). We then ran 10 simulations for each value of B'-B' adhesion between 25 and 50 and recorded screenshots of the resulting structure at 24,000 mcs. The goal in the parameter screen is to identify parameters that achieve the maximal similarity to the in vitro picture, where activated, green B' cells are found in the inner layer and A cells in the outer layer. As shown in Figure 3H, for values of B'-B' adhesion of 35 or higher, the sorting was either incomplete or the two types were randomly mixed. To get a quantitative measure of sorting, we also followed homogeneity index for both type A and B cells (Figure 3I). We calculated a homogeneity index measure inspired from refs 10, 48 and 49 and defined in eq S8 (see Methods and Simulation Quantifications sections) as the average fraction of surface area that cells of type X share with cells of the same type X over their total surface. The measure scores higher if the cells are uniformly contacting cells of the same kind and lower if it has neighbors of a different kind. Given geometrical constraints, the highest value is around 0.8 for our cell numbers (as with a finite number of cells, there will always be

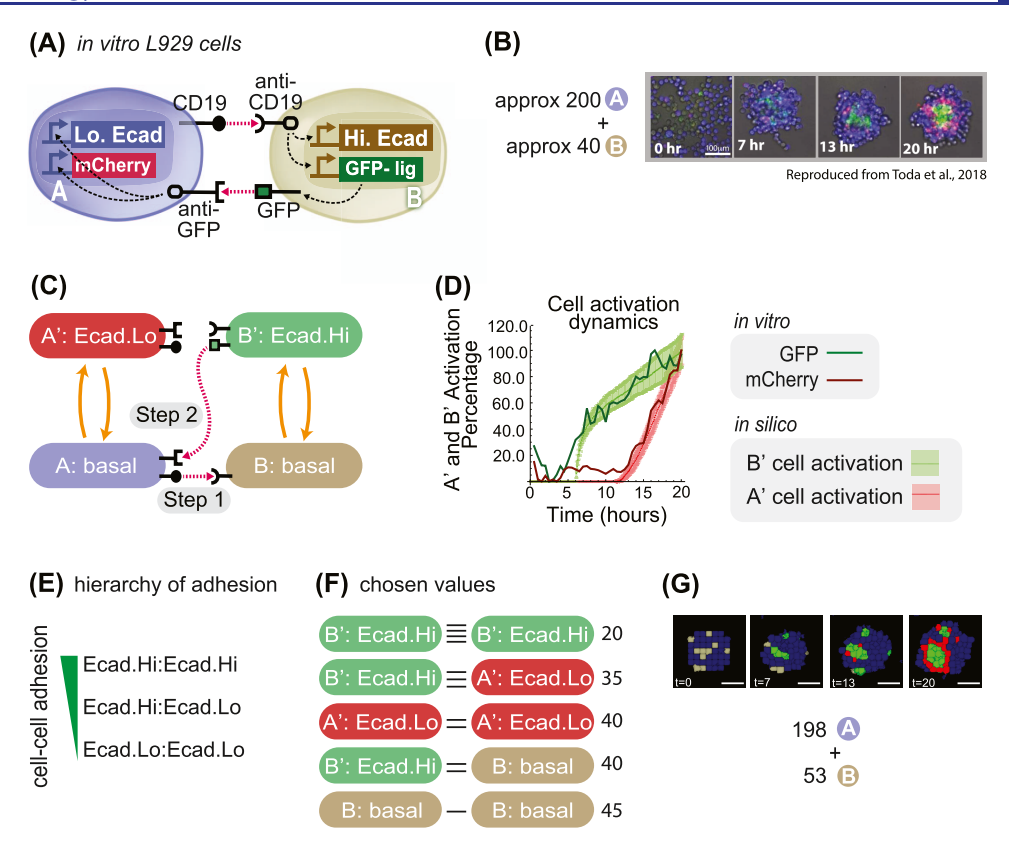


Figure 4. Parameterization of  $A \to B \to A$  network parameters and E-cadherin levels. (A) Diagram 2 cells A (blue) and B (gray) and their signaling with the receptor and promoter representation: cell A has a CD19 ligand (rounded ligand on a stick on the cell membrane of cell A), which activates (pink arrow) the rounded receptor in cell B, which in response activates Hi.E-cad (white rectangle) and GFP-ligand (green rectangle); the GFP-lig (green square on a stick on the membrane) is then produced (gray arrow) on the membrane, which activates the square receptor on cell A that activates intracellularly (white arrows) Lo.E-cad (white rectangle) and mCherry (red rectangle). (B) Experimental results of mixing approximately 200 A cells and 40 B cells; A cells are blue, B cells are gray, B' cells are green, and A' cells are red. (C) State-machine diagram of the network, with the adhesion components. B cell has basal adhesion and rounded receptor; when it is activated by a neighboring rounded receptor, it activates to a B' state where it starts to be adhesive with E-cad.Hi parameter and a square ligand; A cell, blue, has basal adhesion and expresses a rounded ligand and a square receptor; the activation of the square receptor activates A cell to A', which is red and acquires the adhesion of E-cad.Lo parameter. (D) Graph depicting the cell-type activation index over time for activation from  $A \to A'$  in vitro (dark red line) and in silico (light red line and shadowed standard deviation) and from  $B \to B'$  in vitro (dark green line) and in silico (light green line and shadowed standard deviation). We present mean  $\pm$  standard deviation (s.d.) for the *in silico* results (dotted lines with standard deviations in the graph) (n = 30 simulations in silico, n = 1 for in vitro). (E) Hierarchy of adhesion between cells with different levels of E-cadherin adhesion; notation adhesion.level 1: adhesion.level 2 indicates adhesion preference between cells that express adhesion level 1 and cells that express adhesion level 2. (F) Diagram of the cell-cell adhesion strengths for pair-wise cells of different types; horizontal black lines denote cell-cell adhesion, and more horizontal lines denote stronger adhesion. (G) Input (198 A + 53 B cells) and output (developmental trajectory with snapshots at the indicated time frames) of the system with genome as in panel (C). Scale bar is 17.5 pixels in silico, 100 µm in vitro. Microscopic images with a gray background are reproduced from Toda, S.; Blauch, L. R.; Tang, S. K. Y.; Morsut, L.; Lim, W. A. Programming Self-Organizing Multicellular Structures with Synthetic Cell-Cell Signaling. Science 2018, 361 (6398), 156-162. Copyright 2018 AAAS. Reprinted with permission from AAAS.

cells that do not have all their surface in contact with neighbors at all). Following this measure confirmed the impression from the visual inspection that for values of B'-B' adhesion higher than 35, the homogeneity of B/B' cells was low, contrary to what is observed *in vitro* where B/B' has the highest homogeneity (Figure 3I). These results constrained the value of the adhesion of B'-B' when they express E-cad to <35 and we picked the adhesion value for induced E-cad at 25 moving forward.

So far, we kept all of the other adhesion values to the parental level of 49 but wanted to see if this was appropriate. To do so, we performed a similar screen for B–B adhesion values spanning between 25 and 50. In this case, if B–B adhesion is under 40, the sorting of the B cells precedes activation, and only B cells at the interface between B and A cells activate. This leaves the inner core of the B cells to the

inactivated state, which is not what is observed in the *in vitro* counterpart. Therefore, B–B adhesion needs to be higher than 40, and we picked 47. We finally performed a screen for A–A adhesion values; this showed that low values of A–A adhesion results in the formation of a blue core and green poles at the periphery, which is not what is observed *in vitro*. Therefore, A–A adhesion values were constrained to >45 and we picked 49. With these parameters and starting with a mixture of approximately 100 A and 100 B cells, we consistently obtained two-layer structures qualitatively similar to that of the *in vitro* results (see Figures 3J and S1A for quantifications and more replicates and Movie S1).

Collectively then, this screening allowed the identification of a set of adhesion values of B'-B'=25, B-B=47, A-A=49 (reminder that in CompuCell3D lower adhesion values correspond to higher adhesion strengths), which was able to

recapitulate the fully sorted, two-layer spheroid as in the *in vitro* experiment. The choice of the parameters is not univocal; any choice of the parameters in those ranges would have resulted in a two-layer phenotype. We used these values for the rest of the papers for E-cad activation: induced E-cad—induced E-cad = 25; basal E-cad—basal-E-cad = 47, which is consistent with *in vitro* cells in a basal state having a leakiness of E-cad expression even in the absence of activation; <sup>19</sup> this minimal difference between basal and parental (47 *vs* 49) is not sufficient to induce sorting (not shown here, but see Figure S2B.2 for an example where cells with 49 *vs* cells with 45 of adhesion do not sort).

Next, we used the parameter scan approach to parameterize cell-type adhesion for N-cad and P-cad adhesion molecules. For induced N- and P-cadherin, we compared the parameter scan with the in vitro phenotype of a two-layer network where B cells induce N-cad instead of E-cad. The phenotype in vitro is a less well-sorted two-layer (Figure S1B), which is similar to what is obtained in silico with values of B'-B' of around 35. With this parameter, in fact, the homogeneity of B/B' is still higher than the homogeneity of A cells but lower than it was for E-cad expressing cells (compare Figure S1A-B/B' green line with the same line in Figure S1B.4). Hence, for induced Ncad, we chose 35 as adhesion value, and the same was then fixed for induced P-cad (given they are reported to have similar adhesion strengths<sup>47</sup>). Finally, another two-layer structure from the training set allowed parameterization of heterotypic N- and P-cad adhesion, as well as constitutively expressed Pcad. In this circuit, A cells constitutively express low levels of Pcad, whereas B cells are induced to express N-cad (Figure S1C). The resulting phenotype in vitro is that of a spheroid where A cells and B' cells cluster together at different poles. Given the parameter scan in Figure 3H,I, we thought using A-A adhesion values in the range of 35-45 would allow us to achieve that; indeed, when we did simulations with the A-A adhesion set to 43, we obtained in silico structures similar to the in vitro ones, where both A cells and B/B' cells show similar homogeneity index values (Figure S1C). This screening allowed us to identify parameters for adhesion values for E-, N-, and P-cadherin.

Adhesion and Signaling in Three-Layer Networks. More complex three-layer structures can be generated *in vitro* with a more complex signaling network (Figure 4A). In this network architecture, the B cells, when they receive the signal from A, transition to a B' state that is able to communicate back to the A cells that can become activated to A' cells. In this case, A, A', and B' cells have the capacity to both receive and send a signal, a feature known as "transceiver" (Figure 4C). This signaling logic is also called "back-and-forth". This network was used *in vitro* <sup>19</sup> to generate both central symmetric three-layered structures and also noncentral symmetric structures based on the choice of adhesion molecule. We chose to use the central symmetric three-layered structure as a training structure for parameterization *in silico* and leave the noncentral symmetric structures for the test set.

The central symmetric three-layer structure *in vitro* is generated as follows: A and B cell types have basal adhesion deriving from a small amount of leakiness, <sup>19</sup> whereas A' expresses low levels of E-cad (E-cad.Lo) and B' expresses high levels of E-cad (E-cad.Hi). As shown in Figure 4B, when approximately 200 A cells are mixed with approximately 40 B cells *in vitro*, A cells signal to B cells to induce E-cad.Hi, turn on reporter GFP, and form the center of the spheroid.

Subsequently, the surrounding blue A cells expressing blue fluorescence protein (BFP) are activated to A' cells that turn on a red reporter (mCherry) and E-cad.Lo positive *via* signaling coming from activated B' cells, resulting in a three-layered structure with B' cells in the center followed by A' and then A cells at the outside.

To implement this in silico, A cells have ligand A (filled circle) and can respond to ligand B (green square) thanks to the expression of receptor B (squared). B cells have receptor A (rounded) to respond to ligand A and in the B' state can gain the capacity to send ligand B (Figure 4C). To parameterize the signaling for A and B cells, we proceeded as for signaling parameterization in the simper networks described earlier by comparing activation measures in vitro and in silico. For this more complex network architecture, the activation indices are defined based on cell-type conversion from A to A' and B to B' as follows: in vitro, the activation index is the normalized amount of GFP fluorescence (green) for signaling in cell B and of mCherry fluorescence (red) for signaling in cell A (see the Simulation Quantifications section). In silico, the activation index is the normalized ratio of activated cells over the total number of cells of the same type (see Methods and Video Analysis sections). With these definitions, we were able to compare in vitro and in silico signaling and identify parameters for signaling constants as described previously (numerical values for signaling parameters are in Table S1) (Figure 4D). We notice that the signaling parameters that allow for recapitulation of in vitro data set are (slightly) different for cells A and B, even though they have a similar genetic network; we speculate that this could be due, in vitro, to a different level of expression of the receptor or the transgene that makes signaling dynamics different in different cell types; hence, parameterization of different cell types could require parameterization of signaling each time a new circuit is built. We used the identified signaling parameters for all subsequent simulations involving this kind of signaling.

For the adhesion values, the central symmetric three-layer structure involves different expression levels of E-cad protein in different cells, *e.g.*, low levels in A' cells and high levels in B' cells. For the parameterization, based on previous work that established that changes in the expression levels of cadherins change adhesion strength,  $^{24,47}$  we derived a hierarchy as in Figure 4E. Based on this hierarchy, and starting from the previously identified value for E-cad — E-cad of 25, we chose to use E-cad.Lo — E-cad.Lo = 40 and E-cad.Hi — E-cad.Hi = 20 (Figure 4F).

With these parameters for signaling and adhesion, we then simulated the development of a system comprising around 200 A and 50 B initial cells. We observed that there was first induction of B to B' cells, which then formed a green core. Then, the B' cells started to signal to the A cells to turn red (Figures 4G and S2A and Movie S2). At the corresponding time points, we observed structures similar to that of the *in vitro* results (Figure 4B), a three-layer structure consisting of a green B' cell core surrounded by concentric shells of red A' cells and then blue A cells (Figure 4G).

We wondered if, in the signaling scheme, reversion back to the basal state played a role in this trajectory. To test this, we designed networks where there is no reversion, meaning that, once induced, cells cannot revert to the basal state. Qualitatively and *via* homogeneity index, these two scenarios are not distinguishable in our setup (compare Figure S2A with

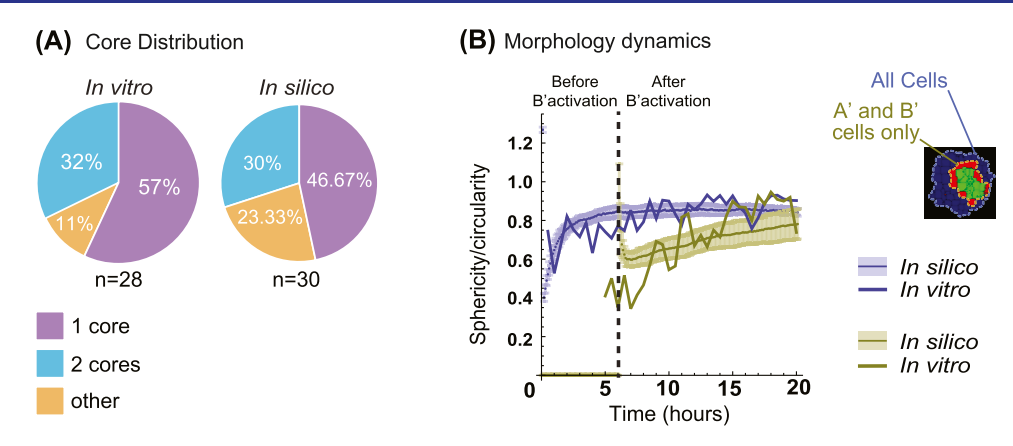


Figure 5. Emergent properties in vitro are captured by the parameterized system in silico for the central symmetric three-layer network. (A) Quantification of the number of cores formed over repeated simulations (n = 30 simulations, n = 28 for in vitro). In vitro result data are from ref 19. See the Methods and Simulation Quantifications sections for more details on core definitions in silico. (B) Quantification of sphericity/circularity indices over the time development of synthetic and in vitro systems (see the Methods and Simulation Quantifications sections for in silico and the Video Analysis section for in vitro details on the indices). In blue, all of the cells are considered; in green, only the activated (A') and (B') cells are considered. The solid line is from in vitro measures; solid lines with shaded contours are from in silico measurements and represent mean and standard deviation intervals, respectively. The vertical dashed line indicates the time of (B') cell activation (n = 30 simulations, n = 1 for in vitro).

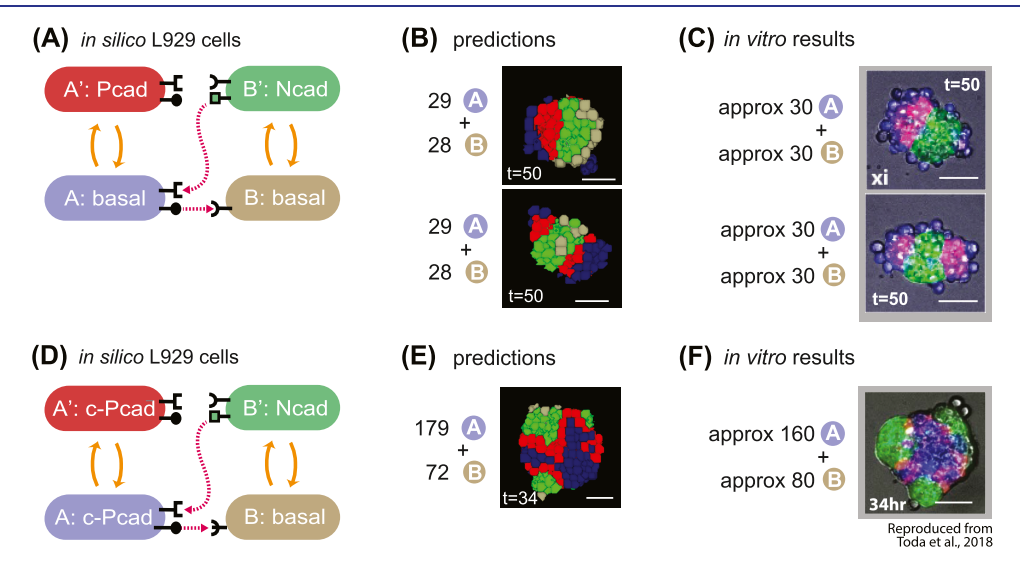


Figure 6. Model correctly predicts the behavior of in vitro experiments with different cadherin target genes. (A) State-machine diagram of the network, with the adhesion components. B cell has basal adhesion and a rounded receptor; when it is activated by a neighboring rounded receptor, it activates to a B' state that is adhesive with N-cad parameter and produces a square ligand; A cell, blue, has basal adhesion and expresses a rounded ligand and a square receptor; the activation of the square receptor activates A cell to A', which is red and has the adhesion of P-cad parameter. (B) Representative results of two classes of resulting structures at t = 50 h of simulated time of approximately 30 A + 30 B cells with the genotype as in panel (A): one class (approx. 10% of the simulations) gives two red poles, and the other class (approx. 90% of the simulations) gives one red pole. See Figure S3 for quantification of homogeneity index over 10 runs of the simulation with the same parameters and initial conditions. (C) In vitro results at t = 50 h of the two categories of structures that are obtained with the genotype of cells in A and with mixing approximately 30 A cells and 30 B cells. (D) State-machine diagram of the network, with the adhesion components. B cell has basal adhesion and a rounded receptor; when it is activated by a neighboring rounded receptor, it activates to a B' state that is adhesive with N-cad parameter and produces a square ligand; A cell, blue, has constitutive P-cad adhesion and expresses a rounded ligand and a square receptor; the activation of the square receptor activates A cell to A', which is red and continues to have adhesion of constitutive P-cad parameter. (E) Representative results of resulting structures at t = 34 hof simulated time of approximately 179 A + 72 B cells with the genotype as in panel (D): a core of blue inactivated A cells, with multiple poles of green activated B' green cells and in the between red activated A' cells. See Figure S3 for the quantification of homogeneity index over 10 runs of the simulation with the same parameters and initial conditions. (F) In vitro results at t = 34 h of a representative structure that is obtained with the genotype of cells in panel (D) and with mixing approximately 160 A cells and 80 B cells. Scale bar is 17.5 pixels = 100  $\mu$ m. Microscopic images with a gray background are reproduced from Toda, S.; Blauch, L. R.; Tang, S. K. Y.; Morsut, L.; Lim, W. A. Programming Self-Organizing Multicellular Structures with Synthetic Cell-Cell Signaling. Science 2018, 361 (6398), 156-162. Copyright 2018 AAAS. Reprinted with permission from AAAS.

Figure S2C), suggesting that, *in silico*, the reversion might not play a big role for this specific trajectory.

Finally, we showed that signaling is necessary for three-layer formation in the *in silico* model, similar to what was shown for the *in vitro* model. In the absence of signaling, there is no

activation to B' and A', no formation of core(s), and no sorting occurring either qualitatively or quantitatively *in silico* (Figure S2B).

This parameterization allowed us to identify values for all of the target parameters that remain unchanged for the rest of the

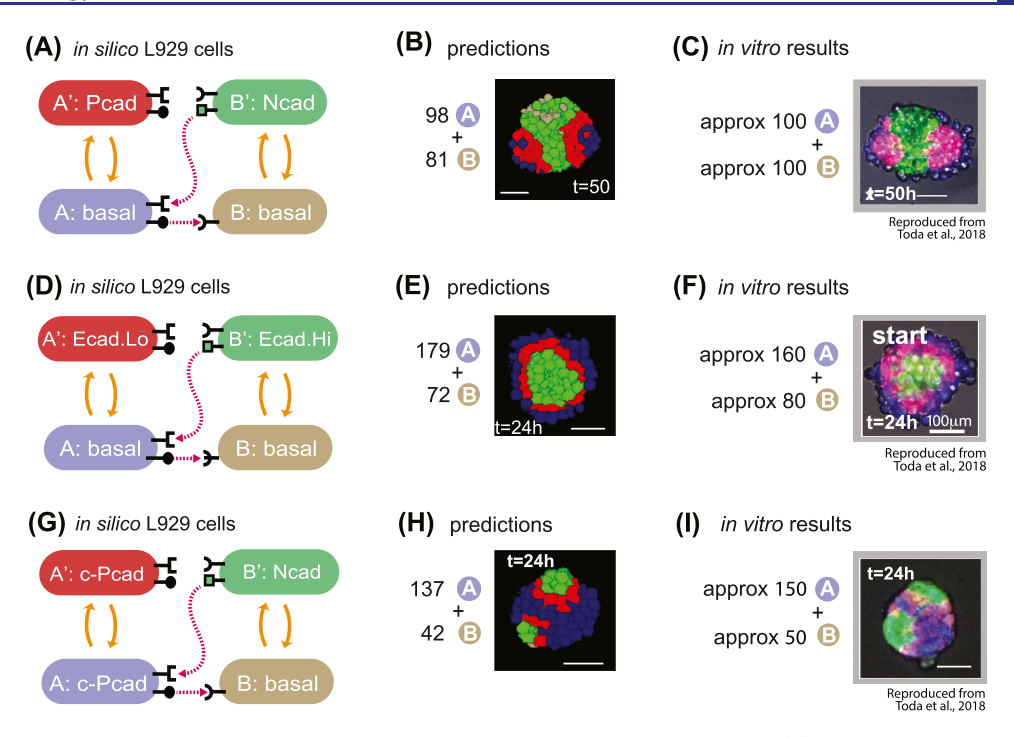


Figure 7. Model correctly predicts the behavior of in vitro experiments with different number of cells. (A) State-machine diagram of the network, with the adhesion components. B cell has basal adhesion and a rounded receptor; when it is activated by a neighboring rounded receptor, it activates to a B' state that is adhesive with N-cad parameter and produces a square ligand; A cell, blue, has basal adhesion and expresses a rounded ligand and a square receptor; the activation of the square receptor activates A cell to A', which is red and has the adhesion of P-cad parameter. (B) Representative results of resulting structures at t = 50 h of simulated time of 98 A + 81 B cells with the genotype as in (A): a core of green activated B' cells, with two poles of red activated A' cells and external to that blue inactivated A cells. See Figure S4 for quantification of homogeneity index over 10 runs of the simulation with the same parameters and initial conditions. (C) In vitro results at t = 50 h of a representative structure that is obtained with the genotype of cells in (A) and with mixing approximately 100 A cells and 100 B cells. Scale bar is 17.5 pixels = 100  $\mu$ m. (D) Statemachine diagram of the network, with the adhesion components. B cell has basal adhesion and a rounded receptor; when it is activated by a neighboring rounded receptor, it activates to a B' state that is adhesive with E-cad. Hi parameter and produces a square ligand; A cell, blue, has basal adhesion and expresses a rounded ligand and a square receptor; the activation of the square receptor activates A cell to A', which is red and has adhesion of E-cad.Lo parameter. (E) Representative result of resulting structures at t = 24 h of the simulated time of approx. 179 A + 72 B cells with the genotype as in (D): a core of green activated B' cells, with a subsequent layer of red A' activated cells, surrounded by a layer of inactivated blue A cells. See Figure S4 for the quantification of homogeneity index over 10 runs of the simulation with the same parameters and initial conditions. (F) In vitro results at t = 24 h of a representative structure that is obtained with the genotype of cells in (D) and with mixing approximately 160 A cells and 80 B cells. Scale bar is 17.5 pixels = 100  $\mu$ m. (G) State-machine diagram of the network, with the adhesion components. B cell has basal adhesion and a rounded receptor; when it is activated by a neighboring rounded receptor, it activates to a B' state that is adhesive with N-cad parameter and produces a square ligand; A cell, blue, has constitutive P-cad adhesion and expresses a rounded ligand and a square receptor; the activation of the square receptor activates A cell to A', which is red and continues to have the adhesion of constitutive P-cad parameter. (H) Representative results of resulting structures at t = 24 h of the simulated time of 137 A + 42 B cells with the genotype as in panel (G): a core of blue inactivated A cells, with multiple poles of green activated B' green cells and in between red activated A' cells. See Figure S4 for the quantification of homogeneity index over 10 runs of the simulation with the same parameters and initial conditions. (I) In vitro results at t = 24 h of a representative structure that is obtained with the genotype of cells in panel (G) and with mixing approximately 150 A cells and 50 B cells. Scale bar is 17.5 pixels = 100 µm. Microscopic images with a gray background are reproduced from Toda, S.; Blauch, L. R.; Tang, S. K. Y.; Morsut, L.; Lim, W. A. Programming Self-Organizing Multicellular Structures with Synthetic Cell-Cell Signaling. Science 2018, 361 (6398), 156-162. Copyright 2018 AAAS. Reprinted with permission from AAAS.

simulations. We then moved to test the quantitative capacity of the newly parameterized model to capture emergent properties of the system.

Testing of Predictive Capacity of the Model in the Testing Set. Parameterized Model Correctly Captures Emergent Properties of In Vitro Developmental Trajectories. With the model parameterized to capture the morphologies and activation dynamics, we wondered if the parameterized model would also reproduce other properties of the *in vitro* systems that were not used to calibrate the model parameters.

As a first example, we focused on the robustness of obtaining the target structures, focusing on the central symmetric threelayer structure. Both the *in vitro* and the *in silico* systems have stochastic components. *In vitro*, the system forms a similar structure with one core 57% of the time experiments performed (n = 28 experiments<sup>19</sup>). In the *in silico* system, the stochasticity comes from the core algorithm in CompuCell3D, as the transition from one stage to the next is shaped by a probability distribution (eq 1). We quantified *in silico* the number of cores formed over repeated simulations of our parameterized model of the central symmetric three-layer structure (n = 30). The majority of the simulations yielded a one-core structure (47%), some yielded a two-core structure (30%), and a minority yielded a noncore structure (23%) (Figure 5A). We compared this distribution to that of morphologies reported for the biological system<sup>19</sup> and found them similar (Pearson  $\chi^2 = 4.75$ , d.f. = 2, P > 0.09).

As a second example, we focused on changes in the quantitative metric of morphology and, in particular, the sphericity of the assembly. *In vitro*, we noticed that the circularity of the structures evolves over time to reach a steady state by the end of the experiment, both for the overall structure and for the cadherin-expressing cells. To quantify these features, we used a standard circularity index in 2D that increases when the structure is more circular (see the Methods and Quantification and Statistical Analyses sections; eq S9) and quantified it over time; results are in Figure 5B, blue and beige solid lines. To compare it with the *in silico* system, we defined a sphericity index *in silico* (eq S7) and measured it over time. We plotted it together with the *in vitro* results and found that they generated qualitatively similar temporal evolution (Figure 5B).

These data collectively show that the parameterized *in silico* system can recapitulate emergent properties of robustness and morphological evolution of the *in vitro* cellular system, properties that have not been used for the identification of the parameters.

Parameterized Model Predicts Developmental Trajectories with Reshuffled Adhesion. We now set out to test the predictive power of the parameterized model for multicellular circuits in the testing set. We start by considering circuits that contain a different combination of adhesion proteins compared to the training set. To do so, with the identified parameters, we ran simulations to see what the model predicts for the behaviors of multicellular systems with genomes that are obtained by changing adhesion values.

In a first example (Figure 6A–C), following the logic of one of the synthetic genomes in the in vitro test set, the in silico implementation had two cell types, A and B, and a back-andforth signaling logic where A activates B to B' and B' activates A to A'. The adhesion features of the cells are basal for cells A and B, whereas A' gains P-cad and B' gains N-cad (Figure 6A). We implemented this program in silico by giving A' cells the value of adhesion that we identified previously for P-cad and similarly with B' cells for the value of adhesion for N-cad. We then ran simulations with  $\sim$ 30 A cells and 30 B cells for 50,000 mcs equivalent to 50 h of in vitro experiment. This gave rise to predicted structures that fell in two categories: one with one green B' pole (90% of the runs) and another with two red A' poles (10% of the runs) (Figure 6B; see also Figure S3A for adhesion matrix, other sample structures, and sorting index dynamics and Movies S3 and S4 for runs with the two different phenotypes). When compared to the in vitro system, these structures display similar classes of morphology (Figure 6C), with the one pole observed more frequently.

We proceeded similarly for a second system (Figure 6D), where the signaling logic is the same back-and-forth signaling between A and B cells, but now P-cad is constitutively expressed in A cells from the beginning, and signaling from B' only changes color from blue to red. When we mixed approximately 160 A and 80 B cells for the equivalent of 34 h, we obtained a structure with B' green cells forming aggregates at polar positions in the spheroid, and the B' aggregates are lined internally by A' red cells; the inactive A cells stay in the center of the aggregate since they express adhesion molecules from the beginning of the experiment (Figures 6E and S3B and Movie S5). The *in vitro* results obtained with engineered cells with a similar genome resulted in a similar architecture (Figure 6F).

These results show that our parameterized model can predict outside of the training set into new genomes obtained by changing the adhesion molecules produced by different cells in the system.

Model Predicts In Vitro Structures When Initial Number of Cells Are Changed. We next explored the computational models' capacity to predict final structures when initial conditions were changed. We ran simulations starting from different amounts of A and B cells for three different systems.

For the first one, using the same underlying genetic architecture as in Figure 6A–C, we increased the initial number of cells to around 90 for both A and B. *In silico*, increasing cell number resulted in a bigger B' green core and the formation of two red poles more systematically (see Figures 7B and S4A for homogeneity index and more replicates and Movie S6). In the *in vitro* experiment, it was noted that when more cells were used, the two-pole phenotype occurred with higher frequency and the B' green core was bigger (Figure 7C) similar to what we obtained *in silico*.

For the second one, we returned to the genetic architecture underlying the central symmetric structure used to parameterize back-and-forth signaling (Figure 7D). Instead of using the initial conditions from the training set (200 A and 40 B), we ran simulations with 160 A and 90 B. We obtained a thicker B' central core and a thinner outer blue layer (Figures 7E and S4B and Movie S7). When we looked at the *in vitro* data, it was noted that this initial cell combination led to a thicker B' core as well (Figure 7F).

For the third one, using the same underlying genetic architecture as in Figure 6D–F, we decreased the initial number of cells to approximately 130 A and 45 B. *In silico*, the result of decreasing number of cells resulted in the formation of two green cores more systematically (see Figures 7H and S4C for homogeneity index and more replicates and Movie S9). In the corresponding test set *in vitro* experiment, a two-pole phenotype is obtained (Figure 7I) similar to what we obtained *in silico*.

These results show that our parameterized model can predict changes to the developmental trajectories when the initial number of cells is changed.

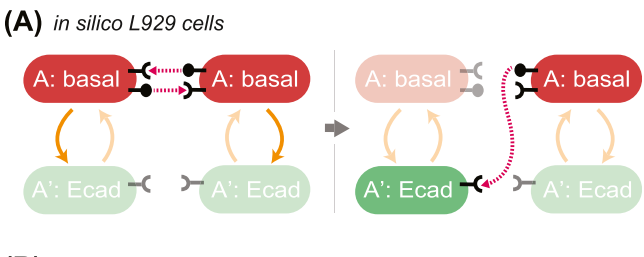
Model Recapitulates Synthetic Structures Generated by Lateral Inhibition Circuits Starting from Genetically Uniform Cell Populations. Having tested prediction capacity for changes in adhesion and changes in initial conditions, we wondered if the system could be predictive when the network itself was changed. To do so, we turned to another test set genome that involved a lateral inhibition signaling network. Lateral inhibition networks are deployed during multicellular development, e.g., in the inner ear, 28 and entail a Notch receptor whose activation results in the repression of its cognate ligand, Delta, in the same cell. This system has been modeled and studied extensively in silico, in vivo, and in vitro. When deployed in architectures in 2D cellular lattices, lateral inhibition networks bifurcate to produce distinctive checkerboard patterning. 7,30,31,50-53 In our computational system, thus far, we had parameterized signaling only for positive activations. Given that in the molecular logic, to obtain inhibitory signaling, there is a swap of an inhibitory transcription factor in place of an activatory one, we hypothesized that our computational model could recapitulate inhibitory signaling by simply modifying our signaling equations (eqs 3.1 and 3.2) such that  $S \rightarrow -S$  (S is signal) and  $\beta \rightarrow -\beta$  (threshold of signaling). This would yield an

inverse relationship between signaling and reporter production, whereby low signaling receiver cells have high reporter production. We tested the inhibition version of the model on lateral inhibition by generating the following network in a monolayer sheet of cells: red A cells send and receive inhibition signals to/from neighboring A cells (Figure S5A). In this setup, the receptor activation decreases the reporter level, so cell state A has a target protein level above the activation threshold (we start from 7000) and can transition to A' if its reporter inhibition is strong enough to make its reporter points fall below the threshold. In the A' state, the cells become green and lose the capacity to signal. When we simulated development starting from red A cells in a singlelayer sheet, we obtained the classic checkerboard pattern of lateral inhibition both when cells are regular (cells are not allowed to move, grow, or divide) or irregular (cells are allowed to move but not grow or divide) (Figure SSB). Importantly, since this was achieved keeping all of the rest of the signaling parameters the same as for the other simulations described so far (adhesions are set at the parental level of 49 for all of the cells), this shows that our parameterization can be extrapolated to simulate other known network contexts.

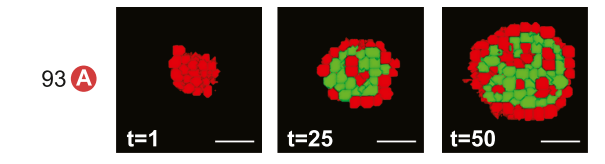
We then moved to see if this implementation of the lateral inhibition network could be used to predict the behaviors of spheroid morphogenesis based on lateral inhibition and changes in cell adhesion. In the in vitro implementation, the logic of the signaling is that of lateral inhibition, but the adhesions are changed: A' fate (green) increases E-cad expression, whereas A cells have basal adhesion capacity (Figure 8C). When we computationally modeled this signaling logic (Figure 8A) starting from approximately 100 A cells, initially some of the red cells become green and then the green cells met each other in the center of the aggregate. After 50 h of simulated time, this results in a spheroid with both A and A' cells, with the A' green cells forming more preferentially the inside of the aggregate and never the outer layer, which was instead populated by inactivated red A cells (see Figures 8B and S8C for robustness and homogeneity index and Movie S8). This phenotype is qualitatively consistent with the observation of the in vitro system, where a two-layered structure is observed with green cells that adhere to other green cells, thereby forming a two-layer structure with a shell of red cells surrounding a green core (Figure 8C).

Collectively, these results show that our parameterized model's predictive capacity can be extended to different network architectures.

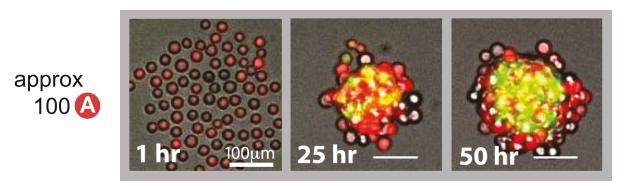
Model-Based Recommendation for Genome for New **Structures.** Finally, we asked if we could identify a network in silico that can give rise to a new structure not yet shown in vitro, a four-layer central symmetric structure (Figure 9A). We started from the observation that increasing the adhesive strength of the gray B cells in the two-layer model resulted in a homogeneous gray core with a thin layer of activated B' cells on the edges (see Figure 3H, middle row, leftmost structure). This resembled a three-layer structure but was done with only a forward signaling between A and B cells. Thus, we hypothesized that if the B-B homotypic adhesion were increased to the inferred B E-cad.Hi adhesive strength, and if the inner B' cells were allowed to activate the outer A cells, we might be able to create a four-layered structure simply by reconfiguring the same synNotch circuits used in previous structures (Figures 9B and S6A). This circuit configuration was tested with different initial conditions consisting of 2:1 mixed







# (C) in vitro results



Reproduced from Toda et al., 2018

Figure 8. Model correctly predicts the behavior of in vitro experiments with different network wiring. (A) State-machine diagram of the network, with the adhesion components. Cells of type A are red and have basal adhesion and express both rounded ligand and receptor; when the receptor is activated enough, it can activate A cells to A' cells, which lose rounded signal expression and gain color green and expression of E-cadherin. (B) Representative results of resulting structures at the indicated timestamp of the developmental trajectory starting from 93 cells of type A with the genotype as in (A); some of the red cells turn green and gather at the center of the core; at t = 50, the external layer is of inactivated A cells, and the internal core is a mixture of mainly green cells with interspersed minority of red cells. See Figure S5 for the quantification of homogeneity index over 10 runs of the simulation with the same parameters and initial conditions. (C) In vitro results at the indicated time points of a representative structure that is obtained with the genotype of cells in (A), starting with 100 A cells. Scale bar is 17.5 pixels = 100  $\mu$ m. Microscopic images are reproduced from Toda, S.; Blauch, L. R.; Tang, S. K. Y.; Morsut, L.; Lim, W. A. Programming Self-Organizing Multicellular Structures with Synthetic Cell-Cell Signaling. Science 2018, 361 (6398), 156-162. Copyright 2018 AAAS. Reprinted with permission from AAAS.

A and B cells at different numbers of cells and allowed to run for 24,000 mcs (equivalent to 24 h in vitro) (Figures 9C and S6B for more replicates). If the initial number of A cells is around 110 and B cells of around 70, there are not enough B cells to sustain the innermost layer, resulting in loss of the innermost layer and forming a three-layer-like structure at the end of the trajectory. If the initial number of A cells is around 1220 and B cells of around 620, however, there are too many cells impeding the formation of the homogeneous inner core of (B/B') cells, resulting in the premature activation of (B/B')cells. In this case, the final structure is composed of multiple, deformed inner cores, each surrounded by a homogeneous layer of A cells. These results indicate that different initial number of cells, with the same circuit, could lead to different morphological outcomes. For the goal of a four-layered structure with a single core, there exists a tradeoff between

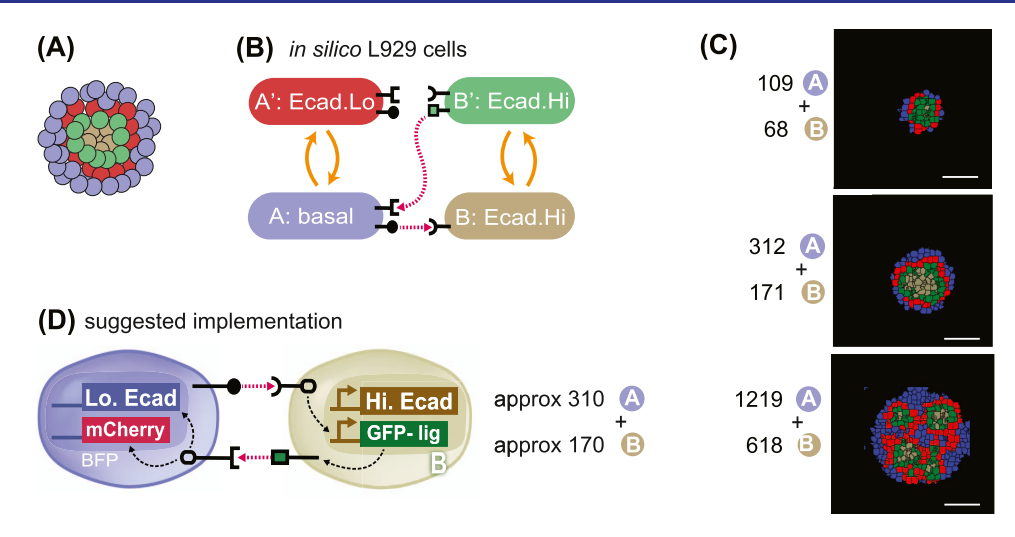


Figure 9. In silico recommendation for obtaining a four-layered structure. (A) Goal target pattern: four layers with gray-green-red-blue cells centrally symmetric. (B) State-machine diagram of the network, with the adhesion components. B cell has adhesion with E-cad.Hi parameter and a rounded receptor; when it is activated by a neighboring rounded receptor, it activates to a B' state that is adhesive with the same E-cad.Hi parameter and produces a square ligand; A cell, blue, has basal adhesion and expresses a rounded ligand and a square receptor; the activation of the square receptor activates A cell to A', which is red and has adhesion of E-cad.Lo parameter. (C) Representative results of resulting structures at t = 24 h of simulated time of cells with the genotype as in (A) and with the ratio and numbers as indicated. All structures generate inactive A cells, activated A' cells, inactive B cells, and activated B' cells in different ratios and in different geometrical arrangements. See Figure S6 for additional replicates over 10 runs of the simulation with the same parameters and initial conditions. (D) Recommended *in vitro* implementation. Scale bar is 17.5 pixels *in silico*, equivalent to approx. 100  $\mu$ m *in vitro*.

the initial number of cells and the resulting homogeneity of the layers in the desired structure. Our *in silico* experiments indicated that an optimal initial number of cells would be around 310 A cells and 170 B cells (Figures 9C and S6B). The recommended circuit would be as depicted in Figure 9D, where A cells have ligand\_A and receptor\_B that activates red and Lo.E-cad expression, whereas B cells have a constitutive expression of Hi.E-cad and receptor\_A that activates ligand\_B expression.

This shows that our computational system can generate recommendations for *in vitro* implementation of circuits for structures that have not been implemented yet.

#### DISCUSSION

A computational framework for the design of genetic networks for synthetic development would allow testing of the reachable morphogenetic space and allow identification of networks for user-defined trajectories and structures that optimize a certain parameter (e.g., burden on cellular machinery, number of cell—cell communication channels, number of cell types, etc.). This preimplementation optimization would provide access to a larger parameter space, allow the identification of less intuitive solutions, and ultimately move the field toward the design phase. Here, we provide a first step in that direction by focusing on a paradigmatic example of synthetic developmental systems, where contact-dependent signaling is paired with changes in cell adhesion in mouse fibroblast cell spheroids.

Networks, where cell—cell signaling changes the mechanical properties of cells, are a recurrent feature of multicellular development. The combination of signaling and morphological effectors has been shown to be at the core of complex developmental transitions: tissues are a complex system where cell—cell signaling affects morphogenesis and then morphogenesis feeds back to influence signaling to robustly generate complex multicellular structures. In fact, the combination of signaling and morphological effectors has been incorporated in

several computational models and shown to be able to replicate the complex morphogenesis of embryonic transitions. 1,9,23 Given that the synthetic morphogenesis described in ref 19 is one of the first synthetic systems that couples chemical and mechanical signaling for synthetic developmental trajectories in mammalian cells, it has attracted other computational descriptions recently, 42,43 with different computational systems or objectives compared to ours. The system in ref 42 describes a similar system in a cellular Potts model, with more focus on the underlying design principles and what can be learned about the logic of these kinds of networks. The system in ref 43 is developed with predictive capacity and with some novel calibration structures and relies on a new computational model for modeling cell movements that is distinct from cellular Potts. We think these efforts will collectively bring the field closer to the goal of rationally designing genetic networks for synthetic developmental trajectories.

Here, we pursued one way to go about developing a computational system for the design of genetic circuits of morphogenesis, using an available data set to train and test our model for cell-cell contact signaling and changes in cell adhesion. The computational system is designed so that it is general in its conception, so that it could be parameterized for different cellular systems, different effectors, different communication systems, etc. In this paper, we show how we parameterized this general computational system to correspond to the synNotch receptor-based communication networks that was previously developed in vitro. 19 The modeling framework itself uses an available open-source platform, CompuCell3D, a cellular Potts-based formalism that allows us to model basic cell behaviors like proliferation, movement, and adhesion-based sorting.<sup>25</sup> Given that this computational system natively retains cell-cell neighboring relationship, which was originally used to compute the "entropy" of a multicellular system, we were able to use it to implement

signaling that is dependent on how much contact there is between "sender" cells and "receiver" cell types. Signaling, in turn, is linked with activation in receiver cells to a different cell type that can be given a different capacity for signaling and/or different levels of adhesion. This allowed us to create a modular backbone for implementing genetic networks based on contact-dependent signaling and changes in cell adhesion, which then generate synthetic developmental trajectories in cells. It would be possible to expand the current system with long-range signaling systems, e.g., since these effectors are available in CompuCell3D.

We parameterized the model with in vitro data using a subset of the complete in vitro data set, what we call the training set. In particular, we parameterized signaling parameters for cellcell contact-dependent synNotch signaling and adhesion values for adhesion molecules of the cadherin family using simple experimental setups. For the signaling, sender-receiver coculture experiments were used. For the adhesion parameters, simple, single-link networks were used, where signaling from A to B induces B to become B' and where the different cell types can have different adhesion molecules. This setup allowed us to explore a parameter space and identify the in silico parameters that most closely mimicked the in vitro structures. The capacity of our system to match experimental results shows that the computational system can be tuned to represent synthetic developmental trajectories. Finally, the signaling for a more complex back-and-forth signaling network was parameterized with a simple example of that type of network in vitro. We used the simplest experiments to parameterize the model, mimicking a future pipeline where simple experiments would provide the baseline parameterization for predictive models that could identify potential circuit architectures for more complex implementations in cells.

Others have done parameterization in different ways: heuristic parametric tuning 42 or machine learning. 43 Our method was to design screenings of parameters in meaningful ranges, motivated by biology and by computational considerations. It allowed us flexibility and exploration of a meaningful parameter space and was able to provide parameters with qualitative and quantitative matching. For more automated processes and extensions, the machine learning parameter estimation is an appealing future direction.

In showing the steps that we took for parameterization, we are also showing how this could be done for different effectors. For example, if one were to be interested in predicting a system where some cells change their proliferation, one would need to parameterize proliferation. To do so, in vitro experiments, where proliferation is quantitatively measured in baseline as well as perturbed conditions, would be set up; parameter tuning would then be performed in silico to identify the proliferation parameters that achieve in silico results similar to the in vitro. This pipeline is shown for cell motility, deformation, synNotch signaling dynamic, and cadherin adhesion in Figure 3.

We then showed that the parameterized model can perform qualitatively accurate predictions of *in vitro* networks from a different subset of the *in vitro* data set, what we call the test set. The test set had either adhesion molecule combination, initial number of cells, or network architecture that were different compared to the parameterization set. The capacity of our model to generalize outside the parameterization set suggests that our parameterization is a valid pipeline, at least for network designs with the same basic building blocks of

signaling and effectors. The capacity to predict different initial conditions is also shown by ref 42. These efforts pave the way toward the computational design of developmental trajectories.

One interesting aspect of our computational system is that it captures some of the robustness features of the *in vitro* system, *e.g.*, in the formation of 1, 2, or multiple cores in the central three-layer structures. Noise and robustness are features of biological systems in general and in particular for developmental systems. S5,56 Given that our computational system is able to capture this important component, it seems it could be a useful resource to approach questions regarding whether certain network architectures are more conducive for buffering noise while still delivering the user-intended structures.

This system can be used to explore the reachable space of morphogenesis with these effectors. An exhaustive characterization of the morphospace has not been attempted here but we think it would be an interesting avenue to pursue.

Finally, we showed how one can go about making a recommendation of a biological network for a user-identified phenotype. The fact that we have a parameterized model and know realistically implementable parameters allowed us to conduct educated searches in a space that is smaller than the entire parameter space. These constrained searches could be helpful when trying to generate user-defined patterns or shapes starting with a limited toolkit of signaling and effector genes. Recent computational research showed that having access to a limited set of primitives is generative of a large number of shapes and patterns if you are allowing free parameter variations.<sup>57</sup> It will be interesting to see if this holds true in parameterized synthetic systems in silico, where you have access to the subset of parameters that are implementable. This would go in parallel with works where unconstrained approaches are taken,<sup>58</sup> which are helpful to identify the needs for novel tools like recombinases in the example. It will also be interesting to see how many of the structures obtained with the multirecombinase approach can be deconstructed and reimplemented in our system with restriction to an implementable toolkit. Ultimately, the test to this kind of use of the modeling framework will come from works where the prediction is followed by implementation to close the cycle.

Our basic framework was built with the goal of designing artificial genetic circuits that would control synthetic developmental trajectories. Given this goal, we focused on "implementable" solutions, i.e., solutions that can be implemented with the available genetic tools. To achieve this, our model modularly exploits the concept of cell types to signify cell transitions based on signaling. These transitions model the acquisition of novel properties following cell-cell signaling events. In the work presented here, cell-type transitions include changes in adhesion or signaling capacity. It would be rather straightforward in our model to extend to have the change in cell types signify changes in proliferation, motility, etc. This expansion would require initial parameterization experiments in a simple setup, so that the user would know the parameters to use, e.g., for the proliferation changes that can be executed with genetic controls.

Another interesting expansion for our system would be the inclusion of other modalities of signaling such as signaling dependent on soluble ligands, bioelectrical signaling, as well as ECM mechanical and chemical signaling. Taking inspiration from what we achieved here with contact-dependent signaling, existing computational solvers for these other types of signaling could be incorporated to add or subtract points to cell-type

transition likelihood. This would be particularly interesting for soluble signaling, as morphogenetic signaling is another family of signaling that is predicated to underlie developmental transitions<sup>54</sup> for which synNotch-based implementation has also been recently reported.<sup>59</sup> Modeling platforms exist to model changes of other morphogenetic currencies, like ECM-based or bioelectrical in a tissue,<sup>60</sup> and one could imagine the extension of our system to calculate cell-type transition based not only on cell—cell contact signaling but also on the input from other computational engines.

Future directions for these computational efforts could be a combination with artificial intelligence-based optimization through either evolutionary algorithms or machine learning. It has been recently shown that these could be used to generate morphologies that can then be recapitulated *in vitro*. 61,62 Algorithms could not only be trained to optimize parameters such as cell line, signaling network, and behavioral response but also incorporate subparameters such as motility, proliferation, differentiability, juxtacrine and soluble morphogen signaling, mechanotransduction, adhesion, chemotaxis, and differentiation, to list a few. Numerous other recent advances in synthetic biology 33,63-70 have made it possible to further control this process, facilitating the synthetic reconstruction of complex native morphogenic processes toward enabling control over custom tissue development.

#### METHODS

Contact for Reagent and Resource Sharing. Further information and requests for resources or codes should be directed to and will be fulfilled by the Lead Contact, Leonardo Morsut (Leonardo.Morsut@med.usc.edu).

Table 1. Key Resources

reagent or resource	source	identifier
software and algorithms		
CompuCell3D (CC3D) v3.7.8	ref 25	RRID:SCR_003052
Mathematica v11.3.0.0	Wolfram Research	RRID:SCR_014448
ImageJ v1.52a	ref 71	RRID:SCR_003070
JMP Pro v14.0.0	SAS Institute	RRID:SCR_014242
Excel v1808	Microsoft	RRID:SCR_016137
General Juxtacrine Signaling Model (GJSM) in CC3D	this paper	N/A

Computational Method Details. CompuCell3D and the Cellular Potts Formalism. We implemented our model in CompuCell3D (CC3D) v.3.7.8,<sup>25</sup> a modeling software that allows simulation of cells and their behaviors using the cellular Potts formalism. By itself, CC3D contains numerous built-in features for replicating *in vitro* cell behavior, several of which we utilized either directly or adjusted *via* CC3D Python v.2.7.13 scripting according to manual v3.7.9. In our model, we incorporated default features from CC3D such as surface area constraint, volume constraint, cell division, adhesion, cell—cell surface contact, and cell types. We implemented custom cell motility, cell growth, and cell signaling, as described below and in subsequent sections.

We defined cells as multipixel entities in 3D that physically act by performing "pixel copy attempts" over simulation time steps (Monte Carlo steps, mcs). Performing "pixel copy attempts" effectively moves and changes both cell geometry and position over time. These pixel copy attempts succeed

probabilistically, determined by the Boltzmann acceptance function,  $P = \mathrm{e}^{-\Delta H/T}$ , where P is the probability of attempt success,  $\Delta H$  is the change in the total effective energy of the system from all attempted pixel copy attempts at the mcs t, and T is the cell motility. <sup>25</sup>

Effective energy (H): because we incorporated the surface area constraint, volume constraint, and adhesion, our total effective energy H at a given mcs t therefore takes the form

$$\begin{split} H &= \sum_{i,j} J_{\sigma(i),\sigma(j)} (1 - \delta_{\sigma(i),\sigma(j)}) + \\ &\sum_{\sigma} \left( \lambda_{\text{Sur}}(\sigma) (\text{Sur}(\sigma) - \text{Sur}_{\text{Tar}}(\sigma))^2 + \lambda_{\text{Vol}}(\sigma) \right. \\ &\left. (\text{Vol}(\sigma) - \text{Vol}_{\text{Tar}}(\sigma))^2 \right) \end{split}$$

as described in ref 3. The terms  $\sigma(i)$  and  $\sigma(j)$  denote the identity of the cells occupying pixel sites i and j separately, with the Kronecker delta limiting the inclusion to only the cell interface. J is a matrix that contains the contact energy between cells of different identities.  $\lambda_{\rm Sur}$  and  $\lambda_{\rm Vol}$  constrain the deviations of a cell from the ideal surface areas  ${\rm Sur}_{\rm Tar}$  and  ${\rm Vol}_{\rm Tar}$ , hereafter referred to as the target surface area and target volume, respectively.

The numerical values in J control adhesion in cellular Potts. The values in J represent a stability index: lower J makes for a more stable state, which is then how you achieve stronger adhesion. Conversely, a higher J leads to weaker adhesion.

Generalized Juxtacrine Signaling Model (GJSM). Juxtacrine signaling is the method employed to achieve the known synthetic structures. For a generic signaling ligand whose expression was constitutive, constant, and unaffected by signaling, we describe the total ligand level, *L*, on a cell's surface by the equation

$$L = \frac{\gamma}{1 + e^{-(t/\xi)}} \tag{S1}$$

where t is the given time in mcs, while  $\gamma$  and  $\xi$  are constants. We chose this equation because of its simplicity. It could be generalized to represent the steady-state ligand level on a cell's surface, recovery of surface ligand level from trypsinization, and experimental conditions such as ligand induction via tetracycline from a drug-controlled promoter (e.g., Tet On).

Then, a receiver cell in contact with the sender cell would change its target protein level, R, by the differential equation (eq 3.1)

$$\frac{\mathrm{d}R}{\mathrm{d}t} = \frac{1}{1 + \mathrm{e}^{-((S-\beta)/\varepsilon)}} - \frac{R}{\kappa}$$

where  $\beta$ ,  $\varepsilon$ , and  $\kappa$  are constants, whereas S is the signal strength. We chose this form for several reasons. First, parameters have intuitive interpretations:  $\beta$  controls sensitivity to S,  $\varepsilon$  modulates the magnitude of S and  $\beta$ , and  $\kappa$  represents the standard linear protein decay rate constant commonly employed in biological models. Second, these parameters have kinetic/biological interpretations due to the logistic function's intrinsic relation to the Hill function. Lastly, this form of the logistic function is easily tunable and well behaved due to its monotonicity from negative infinity to positive infinity and bound between 0 and 1. This tunability is not as easily achievable with the Hill function, where odd or fractional Hill constants lead to the existence of singularities.

In the case where the target gene is a ligand itself, we use eq 2 to calculate ligand levels.

The time-dependent evolution of the reporter, apart from the parameters, depends on signal strength S; this reflects the biological fact that the promoter of the target gene is under the control of the receptor in juxtacrine signaling. Signal strength is itself affected by the number of receptors on the receiver cell  $(\Omega)$ , the number of ligands on contacting neighboring cells (L), and the surface contact area between the receiver cell and its neighbors  $(\Phi)$ . Because these factors evolve over time, S is therefore a morphological dependent and time-dependent function that evolves according to the structure's spatial organization.

The following describes how we take into consideration the shared surface area to compute S. We consider a single receiver cell  $\sigma$ ; first we need to identify which of its neighbors can signal with it. The different cells are assigned different types, according to whether they can signal (ligand expressing) or can receive (receptor expressing) or both. These cell types are indicated as A, A', B, and B' in the text. For example, we have a cell  $\sigma$  of type A that expresses receptor  $r_A$  and that can be activated by ligand  $l_A$ . This allows us to identify the neighbors of sigma by looking through the list of all neighbors of sigma and identifying those that are of a type that bear ligand  $l_A$ .

Then, each different ligand/receptor interaction is treated identically regardless of the specific mechanism (e.g., if it models anti-GFP/GFP or anti-CD19/CD19).

Receiver cells have receptors on their membrane, quantified by  $\Omega_{\sigma}$ . The neighbors have ligands on their membrane, quantified by  $L_i$ . To compute the amount of receptor—ligand interactions that can occur when receiver + cognate sender cells are in contact, we need to calculate the amount of receptor and ligand that are present on the surface of the contact.

To do that, we first define the portion of contact surface for sender (SNi) and receiver (sigma)

$$\Phi_{{\rm SNi}(\sigma)} = \frac{{\rm surface~area~of~contact~between~SNi~and~sigma}}{{\rm Sur}({\rm SN})} \endalign{ \begin{tabular}{c} \end{tabular}} \end{tabular}$$

$$\Phi_{\sigma(i)} = \frac{\text{surface area of contact between SNi and sigma}}{\text{Sur}(\sigma)}$$
 (S2b)

These are now multiplied for the total amount of ligand (or receptor) to obtain the amount of ligand (or receptor) that is available at the area of contact.

Available ligand =  $\Phi_{\mathrm{SNi}(\sigma)} \times L_i$ . Available receptor =  $\Phi_{\sigma(i)} \times \Omega_{\sigma}$ .

With these two values, we can calculate the value of  $S_{\sigma}$  as follows

general: 
$$S_{\sigma} = \sum_{i=1}^{n} \min[(\Phi_{\text{SNi}(\sigma)} \times L_i), (\Phi_{\sigma(i)} \times \Omega_{\sigma})]$$
(S3)

where n is the total number of cells that are currently in contact with sigma and that can engage in signaling with sigma, *i.e.*, produce the ligand for which cell sigma produces the receptor.

This results from the assumption of: a 1-1 stoichiometry of one ligand activating one receptor, given the biochemistry of the signaling; homogeneity of a ligand and receptor on the cell's surface.

This is in general; in the majority of the simulations that we describe in the results, we employed a simplified version where the receptor is considered to be in excess, as we do not have evidence to think otherwise. In this case, the only part of (S3) that is determining the amount of signal S is given by the ligand, so S takes the form of

ligand limiting: 
$$S_{\sigma} = \sum_{i} \Phi_{\text{SNi}(\sigma)} \times L_{i}$$
 (S4)

To implement signaling-inducible behavioral response, we use a state-transition model. We borrow the notation from physics; cells of each genotype, if excitable, bear a ground state and an excited state or even multiple higher-order excited states. The transition between states is regulated by the target gene activation, which is regulated by the cell—cell signaling. Cells in different states can have different properties such as color/state, adhesive properties, deformability properties, signaling/reception capacity (Figure 2F). This quantized representation of cell behavior has been applied, though not with this notation, in other models. 3,4,45 In this way, the signaling can induce behavioral changes in the cells that receive the signal, generating a highly nonlinear system of interacting agents.

Because the reference experiments primarily focus on signaling-inducible adhesion with reporter, we utilize two states per genotype, ground and excited, in the biological replication simulations.

The excited state bears a different color from the ground state, reflecting signaling-induced reporter expression. Adhesion matrix J can be defined for the different states to mirror changes depending on the adhesive strength and binding specificity that the cadherin types in the *in vitro* counterpart express upon sufficient signaling (see Table S1). It is also possible for a cell to fall from the excited state to the ground state due to the loss of signaling; falling under the transition threshold will move an excited-state cell to the ground state, reverting color and excited properties.

In Silico L929 (ISL929) Cell Line Properties. Cell Division. In silico L929 (ISL929) cells consist of multiple pixels and start with a target radius (TR) randomly chosen using a Gaussian distribution ( $\mu = 3.0$  pixels,  $\sigma = 0.5$  pixels). This TR is then used to calculate the target surface area  $(4\pi r^2)$  and target volume  $(4\pi r^3/3)$  for each cell, as in vitro L929 cells adopt a spherical shape at the beginning of experiments. 19 Each cell then undergoes growth by experiencing a net positive increase in TR from small positively skewed uniformly distributed fluctuations in TR. The target surface area and target volume thus increase slowly over time. Upon reaching a threshold volume,  $2 \times 4\pi\mu^3/3$ , the cell then undergoes division, resulting in the original cell and a new cell. The original cell is subsequently reassigned to a new TR from the above Gaussian distribution, and both target surface area and target volume are recalculated. The new cell is assigned the same postdivision parameters as the original cell, modeling completely symmetric cell division. All of the parameters and state variables are inherited by the two daughter cells from the parent cell. These choices result in roughly a doubling time of 24,000 mcs (equivalent to 24 h, the estimated doubling time of L929 cells  $^{19}$ ). For example, this resulted in a ratio of cell number at t= 24 h vs t = 0 h of 2.07  $\pm$  0.10 (n = 10) for simulations in Figure S1A;  $2.02 \pm 0.08$  (n = 10) for simulations in Figure

S1B.5; and the ratio between 20 and 0 h of 1.73  $\pm$  0.08 (n = 30) for Figure 4B.

We note that, due to the stochastic nature of growth, cell death is also possible within this model.

Cell Adhesion. In vitro L929 mouse fibroblasts weakly adhere to one another under ultra-low attachment suspension conditions; <sup>19</sup> thus, we designate our basal, parental ISL929 cells to have a relatively high J to one another and a slightly higher J to the medium, resulting in the formation of weak aggregates in the medium. As a result, these ISL929 cells also bear high motility, again similar to *in vitro* L929. <sup>19,73</sup>

Cell Deformation. Cells that express adhesion proteins and adhere to each other *in vitro* deform markedly and lose their rounded morphology. In CC3D, a way to change deformability of cells is through modulating parameters  $\lambda$  and in eq 1 for H, with lower values corresponding to higher deformability. Cells had an adhesion matrix value of at least 39 (*i.e.*, 0–39 range) (see Table S1), and  $\lambda$  and  $\lambda$  were set to 1.0. Other cells had  $\lambda$  and  $\lambda$  set to 2.2.

*Cell Motility.* Cell motility is defined in CC3D *via* the parameter T. Biologically, it is known that cell adhesion to environment is complexly linked to cell motility, and adhesion effects on motility vary widely between different adhesion proteins and cell types. <sup>74–76</sup> In general, although clearly not all-encompassing, the adhesion abstraction is that strong cell adhesion to environment tends to decrease cell motility. <sup>74,76,77</sup>

For our purposes, in the *in vitro* L929 system, we noticed that the cell motility is rather similar across different cell types and different adhesion, with some minor differences between adherent cells (slightly lower motility) compared with nonadherent cells (slightly higher motility). We therefore defined motility as a sum of a constant  $T_0$  plus function of a cell's environment (neighboring cells and medium), so that higher adhesion results in lower motility; in this way, different cells can have different motilities. Each cell's individual motility  $T_\sigma$  is

$$T_{\sigma} = T_{0} + \zeta \frac{\sum_{\sigma(i)_{i}, j} J_{\sigma(i), \sigma(j)} (1 - \delta_{\sigma(i), \sigma(j)})}{\operatorname{Sur}(\sigma)}$$
(S5)

This formula iterates over each neighboring cell pixel and medium uniquely, and ultimately, *T* is determined only by the type of the focal cell, the types of the neighbors, and total contact with the medium. Categorizing environment by cell types and medium instead, accomplished in CC3D *via* cell—cell surface contact feature and cell-type index, we obtained a computationally simpler approximate formula, which is the one that we use in our simulations

$$T_{\sigma} = T_{0} + \zeta$$

$$\sum_{k} \frac{J_{\text{type}(\sigma), k} \times \text{total contact surface area with } k}{\text{Sur}(\sigma)}$$
(S6)

 $T_0$  is a constant representing basal cell motility,  $\zeta$  is a constant representing how the effectual adhesion is at attenuating motility, and k denotes "cell type" (can be either a cell type or medium). This T allows each cell to sense its adhesivity to the local environment, decreasing motility if adherent to neighbors and restoring motility when exposed to nonadhesive conditions.

 $T_0$  and  $\zeta$  are kept constants throughout after the initial parameterization in Figure 3B.

Simulation Lattice. At the center of a  $100 \times 100 \times 100$  lattice, we seeded a mixture of (A) and (B) cells as a radially symmetric blob to maintain a consistent initial cell aggregate shape while also maintaining a similar cell total and ratio to that of the reference experiment. For the setup in "2D" (Figure S5B), we used a  $100 \times 100 \times 5$  pixel cell monolayer ( $\sim$ 400 cells).

Quantification and Statistical Analyses. Simulation Quantifications. Sphericity Index. (B') green cells were visualized in 3D to determine the core amounts and were counted for each simulation at the end point. Sphericity was measured over time, both for excited states and over all states (Figure 3D), using the formula <sup>78,79</sup>

sphericity = 
$$\frac{\pi^{1/3} (6 \times \text{structure volume})^{2/3}}{\text{structure surface area}}$$
(S7)

We roughly rescaled the sphericity by dividing by 0.48 to compensate for the cubic nature of the voxels. We measured the activation time scale by measuring the number of (B') and (A') cells present per time step and normalized each to 1 maximum.

Homogeneity Index. We were interested in the spatial patterning of different cell types in these multicellular structures over time; thus, we developed and quantified homogeneity index  $\Psi$  per cell-type X, calculated according to the following formula

$$\Psi_{x} = \frac{\sum_{i=1}^{n} \frac{\text{surface area of } \sigma_{i} \text{ that is in contact with cells of type } X}{\text{Sur } (\sigma_{i})}}{n} \tag{S8}$$

where the sum is taken only for cells of type X that are in contact with other cells of type X, and n is the total number of cells of type X in contact with cells of type X.

This measure ranges from 0 to 1, with 1 indicating maximal homogeneity, and is similar to sorting measurements employed in other studies. <sup>10,48,49</sup> By focusing only on cells that have neighbors of the same kind, this measure focuses on clusters and not on isolated cells.

This measure hence depends also on the number of cells present, given that if you only have two cells, *e.g.*, even though they are very homogeneous, less than 100% of their surface will be occupied by the neighbor.

This measure can be generalized for more than one cell type by considering, e.g., two cell types together. For example, in our simulations, when we have a genotype B that gives rise to two cell types (B basal and B' excited), we may be interested in measuring the homogeneity index for B and B' combined. To do so, we calculated  $\Psi_{B,B'}$  by defining type X as {type B or type B'} in the above formula. If desired, this measure can be simply extended to the ground and excited states of each genotype as well,  $\Psi_{A}$ ,  $\Psi_{B}$ ,  $\Psi_{A'}$ ,  $\Psi_{B'}$ , or condensed as desired,  $\Psi_{A,A',B,B'}$ , making it possible to distinguish the effects of different behaviors on morphogenesis. This measure can be applied to many different morphologies, beyond fixed lattices  $^{49}$  and spherical morphologies.

Core Distribution. We counted the number of cores per structure by visualizing only (B') green cells in 3D at the end point of each simulation. To determine whether a core was a single core or double core, we visualized the endpoint simulation (B') green cells from multiple perspectives to prevent viewpoint bias. This allowed us to determine whether there was truly a single core or multiple cores of similar sizes, with the latter generating 2-cores or 3+ cores (counted as

"other" in Figure 5A). Small cell stripe connections between cores were negligible and therefore counted based on the cores. Structures that did not appear core-like (*i.e.*, large cell stripes) were counted in the "other" category (see Figure S7 for examples of core counting).

Activation Index. The activation index in silico is defined as the normalized ratio of activated cells over the total number of cells of the same type, i.e.,  $\#(A')/\text{Max}_t[\#(A')]$  and similarly for (B) and (B') cells.

*Video Analysis. In vitro* data were either provided in the reference paper or obtained by analyzing the supporting video for the counterpart structure from the reference experiments.<sup>19</sup>

Circularity Index. The video was split into constituent frames using Mathematica v11.3.0.0 and then circularity analyzed by drawing a region of interest around the structure using ImageJ v1.52a, both in bright field (all cells) and in merged color field (activated cells only), and data were collated in Microsoft Excel v1808. Circularity was then calculated using the classic equation

circularity = 
$$\frac{4\pi \text{ area}}{\text{perimeter}^2}$$
 (S9)

This measure ranges between 0 and 1, and the closer to 1 indicates it is closer to a perfect circle.

Activation Index. To estimate how fast cells activated over time, we color-separated the green-, red-, and black-merged image portions of each frame by green and red to generate two sets of frames, one for green and one for red, representing, respectively, the activated cells of (B) and (A). We then converted these frames into binary images using the MorphologicalBinarize function in Mathematica, replacing pixels with an intensity above 0.1 with pixels of intensity 1. This threshold value was minimally low to remove noncellular background fluorescence and prevent biasing activated cell detection. Binarization additionally facilitated comparison by splitting in vitro cells into discrete states. Totaling the pixel intensity for each frame of each set estimates the activation per time point for (B) and (A). Cellular background fluorescence, due to a few cells beginning with some green/red, 19 was removed by subtracting the minimum background fluorescence of the time series. Using the minimum helped negate cellular background fluorescence with again minimal biasing of activated cell detection.

Statistical Analyses. Sample sizes are given in the text and/or figure caption. Statistical tests were performed in JMP PRO v14.0.0 with a significance level of 0.05. We performed a  $\chi^2$  analysis for our core distribution analyses (Figures 5A and S2C.4). An appropriate test was chosen according to data type, and assumptions were tested by residual analysis. We report and show mean  $\pm$  s.d. for all measures.

# ASSOCIATED CONTENT

## Supporting Information

The Supporting Information is available free of charge at https://pubs.acs.org/doi/10.1021/acssynbio.0c00369.

Table with signaling and simulation parameters (Tables S1) (XLSX)

Table with adhesion parameters (Tables S2) (PDF)

In silico formation of two-layer structure (Movie S1)
(MP4)

In silico formation of three-layer structure (Movie S2) (MP4)

In silico predicted developmental trajectory with shuffled adhesion, related to Figure 6A–C (Movie S3) (MP4) In silico predicted developmental trajectory with shuffled adhesion, related to Figure 6A–C (Movie S4) (MP4) In silico predicted developmental trajectory with shuffled adhesion, related to Figure 6D–F (Movie S5) (MP4) In silico predicted developmental trajectory with different initial number of cells, related to Figure 7A–C (Movie S6) (MP4)

In silico predicted developmental trajectory with different initial number of cells, related to Figure 7D–F (Movie S7) (MP4)

In silico predicted developmental trajectory with different initial number of cells, related to Figure 8 (Movie S8) (MP4)

In silico predicted developmental trajectory with shuffled adhesion, related to Figure 7G–I (Movie S9) (MP4) Additional experimental details (Figures S1–S6); additional details on methods (Figure S7) (PDF)

## AUTHOR INFORMATION

#### **Corresponding Authors**

Calvin Lam — Eli and Edythe Broad CIRM Center,
Department of Stem Cell Biology and Regenerative Medicine,
Keck School of Medicine, University of Southern California,
Los Angeles, California 90033-9080, United States; Present
Address: College of Medicine, University of Nebraska
Medical Center, Omaha, Nebraska 68198-0001, United
States; Email: calvin.lam.k@gmail.com

Leonardo Morsut — Eli and Edythe Broad CIRM Center,
Department of Stem Cell Biology and Regenerative Medicine,
Keck School of Medicine, University of Southern California,
Los Angeles, California 90033-9080, United States;
Department of Biomedical Engineering, Viterbi School of
Engineering, University of Southern California, Los Angeles,
California 90089-1111, United States; orcid.org/00000001-7049-3478; Email: Leonardo.Morsut@med.usc.edu

#### **Authors**

Sajeev Saluja — Eli and Edythe Broad CIRM Center,
Department of Stem Cell Biology and Regenerative Medicine,
Keck School of Medicine, University of Southern California,
Los Angeles, California 90033-9080, United States; Present
Address: Verily Life Sciences, 269 East Grand Avenue,
South San Francisco, California 94080, United States.;
orcid.org/0000-0002-5191-1897

George Courcoubetis — Department of Physics and Astronomy, University of Southern California, Los Angeles, California 90089-0484, United States; Present Address: Convergent Science Institute in Cancer, Michelson Center for Convergent Bioscience, University of Southern California, Los Angeles, California 90089, United States

Dottie Yu — Eli and Edythe Broad CIRM Center, Department of Stem Cell Biology and Regenerative Medicine, Keck School of Medicine, University of Southern California, Los Angeles, California 90033-9080, United States

Christian Chung — Eli and Edythe Broad CIRM Center,
Department of Stem Cell Biology and Regenerative Medicine,
Keck School of Medicine, University of Southern California,
Los Angeles, California 90033-9080, United States;
orcid.org/0000-0001-9281-4439

Josquin Courte — Eli and Edythe Broad CIRM Center, Department of Stem Cell Biology and Regenerative Medicine, Keck School of Medicine, University of Southern California, Los Angeles, California 90033-9080, United States

Complete contact information is available at: https://pubs.acs.org/10.1021/acssynbio.0c00369

## **Author Contributions**

C.L., S.S., and G.C. contributed equally to this paper. Conceptualization: C.L. and L.M.; methodology: C.L., L.M., S.S., G.C., J.C., C.C., and D.Y.; software: C.L. and S.S.; validation: C.L., S.S., and G.C.; formal analysis: C.L. and G.C.; investigation: C.L., S.S., and G.C.; resources: L.M.; data curation: C.L., S.S., and G.C.; writing—original draft: C.L. and L.M.; writing—review and editing: C.L., L.M., S.S., and G.C.; visualization: C.L., L.M., S.S., and G.C.; supervision: L.M.; project administration: L.M.; and funding acquisition: L.M.

#### **Notes**

The authors declare the following competing financial interest(s): L.M. is a coinventor of synNotch, which was licensed to Cell Design Labs (acquired by Gilead), and receives royalty payments for this from UCSF.

<sup>V</sup>Lead contact.

All simulations were performed in CompuCell3D v3.7.8 with custom scripts coded in Python v2.7.13. General source codes and specific codes for the structures presented in this study are available at [https://github.com/lmorsut/Lam\_Morsut\_GJSM]. Data sets for the structures are available upon request.

## ACKNOWLEDGMENTS

The authors are grateful to the developers of CompuCell3D and the users of the help forum for their assistance in learning the program. The authors would also like to thank Marion Johnson and the other members of the Morsut lab, members of the USC stem cell department, Dr. Matt Thomson, members of the Thomson lab at Caltech, and the anonymous reviewers for feedback on the project and the manuscript that improved the work. The authors thank Amanda Frataccia for her work on the scientific illustration of the project and also their family and friends that support them always and in particular for the times of review of this work that took place during the COVID-19 pandemic. This project was supported by a National Institute of Biomedical Imaging and Bioengineering R00 to L.M. (4R00EB021030-03), NSF RECODE from CBET-2034495, R35 from NIGMS R35 GM138256, along with a USC Department of Stem Cell Biology and Regenerative Medicine Startup Fund.

## REFERENCES

- (1) Marin-Riera, M.; Moustakas-Verho, J.; Savriama, Y.; Jernvall, J.; Salazar-Ciudad, I. Differential Tissue Growth and Cell Adhesion Alone Drive Early Tooth Morphogenesis: An Ex Vivo and in Silico Study. *PLoS Comput. Biol.* **2018**, *14*, No. e1005981.
- (2) Lambert, B.; MacLean, A. L.; Fletcher, A. G.; Combes, A. N.; Little, M. H.; Byrne, H. M. Bayesian Inference of Agent-Based Models: A Tool for Studying Kidney Branching Morphogenesis. *J. Math. Biol.* **2018**, *76*, 1673–1697.
- (3) Hester, S. D.; Belmonte, J. M.; Gens, J. S.; Clendenon, S. G.; Glazier, J. A. A Multi-Cell, Multi-Scale Model of Vertebrate Segmentation and Somite Formation. *PLoS Comput. Biol.* **2011**, *7*, No. e1002155.

- (4) Hutson, M. S.; Leung, M. C. K.; Baker, N. C.; Spencer, R. M.; Knudsen, T. B. Computational Model of Secondary Palate Fusion and Disruption. *Chem. Res. Toxicol.* **2017**, *30*, 965–979.
- (5) Lakatos, D.; Somfai, E.; Méhes, E.; Czirók, A. Soluble VEGFR1 Signaling Guides Vascular Patterns into Dense Branching Morphologies. J. Theor. Biol. 2018, 456, 261–278.
- (6) Lin, C.-M.; Jiang, T. X.; Baker, R. E.; Maini, P. K.; Widelitz, R. B.; Chuong, C.-M. Spots and Stripes: Pleomorphic Patterning of Stem Cells via p-ERK-Dependent Cell Chemotaxis Shown by Feather Morphogenesis and Mathematical Simulation. *Dev. Biol.* **2009**, 334, 369–382.
- (7) Shaya, O.; Binshtok, U.; Hersch, M.; Rivkin, D.; Weinreb, S.; Amir-Zilberstein, L.; Khamaisi, B.; Oppenheim, O.; Desai, R. A.; Goodyear, R. J.; Richardson, G. P.; Chen, C. S.; Sprinzak, D. Cell-Cell Contact Area Affects Notch Signaling and Notch-Dependent Patterning. *Dev. Cell* **2017**, *40*, 505.e6–511.e6.
- (8) Swat, M. H.; Thomas, G. L.; Shirinifard, A.; Clendenon, S. G.; Glazier, J. A. Emergent Stratification in Solid Tumors Selects for Reduced Cohesion of Tumor Cells: A Multi-Cell, Virtual-Tissue Model of Tumor Evolution Using CompuCell3D. *PLoS One* **2015**, *10*, No. e0127972.
- (9) Belmonte, J. M.; Clendenon, S. G.; Oliveira, G. M.; Swat, M. H.; Greene, E. V.; Jeyaraman, S.; Glazier, J. A.; Bacallao, R. L. Virtual-Tissue Computer Simulations Define the Roles of Cell Adhesion and Proliferation in the Onset of Kidney Cystic Disease. *Mol. Biol. Cell* **2016**, *27*, 3673–3685.
- (10) Flenner, E.; Marga, F.; Neagu, A.; Kosztin, I.; Forgacs, G. Relating Biophysical Properties Across Scales. In *Multiscale Modeling of Developmental Systems*; Schnell, S.; Maini, P. K.; Newman, S. A.; Newman, T. J., Eds.; Current Topics in Developmental Biology; Academic Press, 2008; Vol. 81, pp 461–483.
- (11) Newman, S. A. Form and Function Remixed: Developmental Physiology in the Evolution of Vertebrate Body Plans: Evolution of Vertebrate Body Plans. *J. Physiol.* **2014**, *592*, 2403–2412.
- (12) Newman, S. A. Physico-Genetic Determinants in the Evolution of Development. *Science* **2012**, *338*, 217–219.
- (13) Ho, C.; Morsut, L. Novel Synthetic Biology Approaches for Developmental Systems. *Stem Cell Rep.* **2021**, *16*, 1051–1064.
- (14) Davies, J. Using Synthetic Biology to Explore Principles of Development. *Development* **2017**, *144*, 1146–1158.
- (15) Ebrahimkhani, M. R.; Ebisuya, M. Synthetic Developmental Biology: Build and Control Multicellular Systems. *Curr. Opin. Chem. Biol.* **2019**, *52*, 9–15.
- (16) Santorelli, M.; Lam, C.; Morsut, L. Synthetic Development: Building Mammalian Multicellular Structures with Artificial Genetic Programs. *Curr. Opin. Biotechnol.* **2019**, *59*, 130–140.
- (17) Schlissel, G.; Li, P. Synthetic Developmental Biology: Understanding Through Reconstitution. *Annu. Rev. Cell Dev. Biol.* **2020**, *36*, 339–357.
- (18) Teague, B. P.; Guye, P.; Weiss, R. Synthetic Morphogenesis. Cold Spring Harbor Perspect. Biol. 2016, 8, No. a023929.
- (19) Toda, S.; Blauch, L. R.; Tang, S. K. Y.; Morsut, L.; Lim, W. A. Programming Self-Organizing Multicellular Structures with Synthetic Cell-Cell Signaling. *Science* **2018**, *361*, 156–162.
- (20) Toda, S.; Brunger, J. M.; Lim, W. A. Synthetic Development: Learning to Program Multicellular Self-Organization. *Curr. Opin. Syst. Biol.* **2019**, *14*, 41–49.
- (21) Chan, C. J.; Heisenberg, C.-P.; Hiiragi, T. Coordination of Morphogenesis and Cell-Fate Specification in Development. *Curr. Biol.* **2017**, 27, R1024–R1035.
- (22) Hannezo, E.; Heisenberg, C.-P. Mechanochemical Feedback Loops in Development and Disease. *Cell* **2019**, *178*, 12–25.
- (23) Urdy, S. On the Evolution of Morphogenetic Models: Mechano-Chemical Interactions and an Integrated View of Cell Differentiation, Growth, Pattern Formation and Morphogenesis. *Biol. Rev.* **2012**, *87*, 786–803.
- (24) Foty, R. A.; Steinberg, M. S. The Differential Adhesion Hypothesis: A Direct Evaluation. *Dev. Biol.* **2005**, 278, 255–263.

- (25) Swat, M. H.; Thomas, G. L.; Belmonte, J. M.; Shirinifard, A.; Hmeljak, D.; Glazier, J. A. Multi-Scale Modeling of Tissues Using CompuCell3D. In *Computational Methods in Cell Biology*; Asthagiri, A. R.; Arkin, A. P., Eds.; Methods in Cell Biology; Academic Press: 2012; Chapter 13, Vol. 110, pp 325–366.
- (26) Bocci, F.; Onuchic, J. N.; Jolly, M. K. Understanding the Principles of Pattern Formation Driven by Notch Signaling by Integrating Experiments and Theoretical Models. *Front. Physiol.* **2020**, *11*, No. 929.
- (27) Reichrath, J.; Reichrath, S. Notch Signaling and Embryonic Development: An Ancient Friend, Revisited. In *Notch Signaling in Embryology and Cancer*; Reichrath, J.; Reichrath, S., Eds.; Advances in Experimental Medicine and Biology; Springer International Publishing: Cham, 2020; Vol. 1218, pp 9–37.
- (28) Daudet, N.; Żak, M. Notch Signalling: The Multitask Manager of Inner Ear Development and Regeneration. In *Notch Signaling in Embryology and Cancer*; Reichrath, J.; Reichrath, S., Eds.; Advances in Experimental Medicine and Biology; Springer International Publishing: Cham, 2020; Vol. 1218, p 129–157.
- (29) Murata, J.; Ikeda, K.; Okano, H. Notch Signaling and the Developing Inner Ear. In *Notch Signaling in Embryology and Cancer*; Reichrath, J.; Reichrath, S., Eds.; Advances in Experimental Medicine and Biology; Springer US: New York, NY, 2012; Vol. 727, pp 161–173.
- (30) Ghosh, R.; Tomlin, C. J. In Lateral Inhibition through Delta-Notch Signaling: A Piecewise Affine Hybrid Model BT—Hybrid Systems: Computation and Control; Di Benedetto, M. D.; Sangiovanni-Vincentelli, A., Eds.; Springer: Berlin, Heidelberg, 2001; pp 232–246.
- (31) Sprinzak, D.; Lakhanpal, A.; LeBon, L.; Garcia-Ojalvo, J.; Elowitz, M. B. Mutual Inactivation of Notch Receptors and Ligands Facilitates Developmental Patterning. *PLoS Comput. Biol.* **2011**, 7, No. e1002069.
- (32) Bosenberg, M. W.; Massagué, J. Juxtacrine Cell Signaling Molecules. *Curr. Opin. Cell Biol.* **1993**, *5*, 832–838.
- (33) Morsut, L.; Roybal, K. T.; Xiong, X.; Gordley, R. M.; Coyle, S. M.; Thomson, M.; Lim, W. A. Engineering Customized Cell Sensing and Response Behaviors Using Synthetic Notch Receptors. *Cell* **2016**, *164*, 780–791.
- (34) Cameron, D. E.; Bashor, C. J.; Collins, J. J. A Brief History of Synthetic Biology. *Nat. Rev. Microbiol.* **2014**, *12*, 381–390.
- (35) Meng, F.; Ellis, T. The Second Decade of Synthetic Biology: 2010-2020. Nat. Commun. 2020, 11, No. 5174.
- (36) Way, J. C.; Collins, J. J.; Keasling, J. D.; Silver, P. A. Integrating Biological Redesign: Where Synthetic Biology Came From and Where It Needs to Go. *Cell* **2014**, *157*, 151–161.
- (37) Nielsen, A. A. K.; Der, B. S.; Shin, J.; Vaidyanathan, P.; Paralanov, V.; Strychalski, E. A.; Ross, D.; Densmore, D.; Voigt, C. A. Genetic Circuit Design Automation. *Science* **2016**, *352*, No. aac7341.
- (38) Muldoon, J. J.; Kandula, V.; Hong, M.; Donahue, P. S.; Boucher, J. D.; Bagheri, N.; Leonard, J. N. Model-Guided Design of Mammalian Genetic Programs. *Sci. Adv.* **2020**, No. eabe9375.
- (39) Blackiston, D.; Lederer, E.; Kriegman, S.; Garnier, S.; Bongard, J.; Levin, M. A Cellular Platform for the Development of Synthetic Living Machines. *Sci. Rob.* **2021**, *6*, No. eabf1571.
- (40) Kriegman, S.; Blackiston, D.; Levin, M.; Bongard, J. A Scalable Pipeline for Designing Reconfigurable Organisms. *Proc. Natl. Acad. Sci. U.S.A.* **2020**, *117*, 1853–1859.
- (41) Libby, A. R. G.; Briers, D.; Haghighi, I.; Joy, D. A.; Conklin, B. R.; Belta, C.; McDevitt, T. C. Automated Design of Pluripotent Stem Cell Self-Organization. *Cell Syst.* **2019**, *9*, 483.e10–495.e10.
- (42) Mulberry, N.; Edelstein-Keshet, L. Self-Organized Multicellular Structures from Simple Cell Signaling: A Computational Model. *Phys. Biol.* **2020**, *17*, No. 066003.
- (43) Sivakumar, N.; Warner, H. V.; Peirce, S. M.; Lazzara, M. J. A Computational Modeling Approach for Predicting Multicell Patterns Based on Signaling-Induced Differential Adhesion. *Syst. Biol.* **2021**, DOI: 10.1101/2021.08.05.455232.
- (44) Hernandez-Lopez, R. A.; Yu, W.; Cabral, K. A.; Creasey, O. A.; del Lopez Pazmino, M.; Tonai, Y.; De Guzman, A.; Mäkelä, A.;

- Saksela, K.; Gartner, Z. J.; Lim, W. A. T Cell Circuits That Sense Antigen Density with an Ultrasensitive Threshold. *Science* **2021**, *371*, 1166–1171.
- (45) Anderson, A. R. A. A Hybrid Mathematical Model of Solid Tumour Invasion: The Importance of Cell Adhesion. *Math. Med. Biol.: J. IMA* **2005**, 22, 163–186.
- (46) Hester, S. D.; Belmonte, J. M.; Gens, J. S.; Clendenon, S. G.; Glazier, J. A. A Multi-Cell, Multi-Scale Model of Vertebrate Segmentation and Somite Formation. *PLoS Comput. Biol.* **2011**, 7, No. e1002155.
- (47) Duguay, D.; Foty, R. A.; Steinberg, M. S. Cadherin-Mediated Cell Adhesion and Tissue Segregation: Qualitative and Quantitative Determinants. *Dev. Biol.* **2003**, 253, 309–323.
- (48) Sun, Y.; Wang, Q. Modeling and Simulations of Multicellular Aggregate Self-Assembly in Biofabrication Using Kinetic Monte Carlo Methods. *Soft Matter* **2013**, *9*, 2172–2186.
- (49) Olimpio, E. P.; Dang, Y.; Youk, H. Statistical Dynamics of Spatial-Order Formation by Communicating Cells. *iScience* **2018**, *2*, 27–40.
- (50) Collier, J. R.; Monk, N. A. M.; Maini, P. K.; Lewis, J. H. Pattern Formation by Lateral Inhibition with Feedback: A Mathematical Model of Delta-Notch Intercellular Signalling. *J. Theor. Biol.* **1996**, 183, 429–446.
- (51) Cohen, M.; Georgiou, M.; Stevenson, N. L.; Miodownik, M.; Baum, B. Dynamic Filopodia Transmit Intermittent Delta-Notch Signaling to Drive Pattern Refinement during Lateral Inhibition. *Dev. Cell* **2010**, *19*, 78–89.
- (52) Sprinzak, D.; Lakhanpal, A.; LeBon, L.; Santat, L. A.; Fontes, M. E.; Anderson, G. A.; Garcia-Ojalvo, J.; Elowitz, M. B. Cis-Interactions between Notch and Delta Generate Mutually Exclusive Signalling States. *Nature* **2010**, *465*, 86–90.
- (53) Simakov, D. S. A.; Pismen, L. M. Discrete Model of Periodic Pattern Formation through a Combined Autocrine—Juxtacrine Cell Signaling. *Phys. Biol.* **2013**, *10*, No. 046001.
- (54) Gilmour, D.; Rembold, M.; Leptin, M. From Morphogen to Morphogenesis and Back. *Nature* **2017**, *541*, 311–320.
- (55) Gursky, V. V.; Surkova, S. Y.; Samsonova, M. G. Mechanisms of Developmental Robustness. *Biosystems* **2012**, *109*, 329–335.
- (56) Dong, P.; Liu, Z. Shaping Development by Stochasticity and Dynamics in Gene Regulation. *Open Biol.* **2017**, *7*, No. 170030.
- (57) Hagolani, P. F.; Zimm, R.; Marin-Riera, M.; Salazar-Ciudad, I. Cell Signaling Stabilizes Morphogenesis against Noise. *Development* **2019**, *146*, No. dev179309.
- (58) Appleton, E.; Mehdipour, N.; Daifuku, T.; Briers, D.; Haghighi, I.; Moret, M.; Chao, G.; Wannier, T.; Chiappino-Pepe, A.; Huang, J.; Belta, C.; Church, G. Genetic Design Automation for Autonomous Formation of Multicellular Shapes from a Single Cell Progenitor. *Synth. Biol.* **2019**, DOI: 10.1101/807107.
- (59) Toda, S.; McKeithan, W. L.; Hakkinen, T. J.; Lopez, P.; Klein, O. D.; Lim, W. A. Engineering Synthetic Morphogen Systems That Can Program Multicellular Patterning. *Science* **2020**, *370*, 327–331.
- (60) Pietak, A.; Levin, M. Exploring Instructive Physiological Signaling with the Bioelectric Tissue Simulation Engine. *Front. Bioeng. Biotechnol.* **2016**, *4*, No. 55.
- (61) Briers, D.; Libby, A. R.G.; Haghighi, I.; Joy, D. A.; Conklin, B. R.; Belta, C.; McDevitt, T. C. Self-Organized Pluripotent Stem Cell Patterning by Automated Design. *Cell Syst.* **2019**, *9*, 483–495.
- (62) Kriegman, S.; Blackiston, D.; Levin, M.; Bongard, J. A Scalable Pipeline for Designing Reconfigurable Organisms. *Proc. Natl. Acad. Sci. U.S.A.* **2019**, 1853.
- (63) Hartfield, R. M.; Schwarz, K. A.; Muldoon, J. J.; Bagheri, N.; Leonard, J. N. Multiplexing Engineered Receptors for Multiparametric Evaluation of Environmental Ligands. *ACS Synth. Biol.* **2017**, *6*, 2042–2055
- (64) Daringer, N. M.; Dudek, R. M.; Schwarz, K. A.; Leonard, J. N. Modular Extracellular Sensor Architecture for Engineering Mammalian Cell-Based Devices. ACS Synth. Biol. 2014, 3, 892.
- (65) Barnea, G.; Strapps, W.; Herrada, G.; Berman, Y.; Ong, J.; Kloss, B.; Axel, R.; Lee, K. J. The Genetic Design of Signaling

Cascades to Record Receptor Activation. *Proc. Natl. Acad. Sci. U.S.A.* **2008**, *105*, 64–69.

- (66) Conklin, B. R.; Hsiao, E. C.; Claeysen, S.; Dumuis, A.; Srinivasan, S.; Forsayeth, J. R.; Guettier, J.-M.; Chang, W. C.; Pei, Y.; McCarthy, K. D.; Nissenson, R. A.; Wess, J.; Bockaert, J.; Roth, B. L. Engineering GPCR Signaling Pathways with RASSLs. *Nat. Methods* **2008**, *5*, 673–678.
- (67) Scheller, L.; Strittmatter, T.; Fuchs, D.; Bojar, D.; Fussenegger, M. Generalized Extracellular Molecule Sensor Platform for Programming Cellular Behavior Leo. *Nat. Chem. Biol.* **2018**, *14*, 723.
- (68) Baeumler, T. A.; Ahmed, A. A.; Fulga, T. A. Engineering Synthetic Signaling Pathways with Programmable DCas9-Based Chimeric Receptors. *Cell Rep.* **2017**, *20*, 2639–2653.
- (69) Qudrat, A.; Truong, K. Engineering Synthetic Proteins to Generate Ca2+ Signals in Mammalian Cells. *ACS Synth. Biol.* **2017**, *6*, 582–590.
- (70) Qudrat, A.; Truong, K. Antibody-Based Fusion Proteins Allow Ca2+ Rewiring to Most Extracellular Ligands. *ACS Synth. Biol.* **2017**, 531
- (71) Schneider, C. A.; Rasband, W. S.; Eliceiri, K. W. NIH Image to Image]: 25 Years of Image Analysis. *Nat. Methods* **2012**, *9*, 671–675.
- (72) Reeve, R.; Turner, J. R. Pharmacodynamic Models: Parameterizing the Hill Equation, Michaelis-Menten, the Logistic Curve, and Relationships Among These Models. *J. Biopharm. Stat.* **2013**, 23, 648–661.
- (73) Persson, J.; Mölder, A. L.; Pettersson, S.-G.; Alm, K. Cell Motility Studies Using Digital Holographic Microscopy. *Microscopy: Sci., Technol., Appl. Educ.* **2010**, 1063.
- (74) Gumbiner, B. M. Cell Adhesion: The Molecular Basis of Tissue Architecture and Morphogenesis. *Cell* **1996**, *84*, 345–357.
- (75) Nieman, M. T.; Prudoff, R. S.; Johnson, K. R.; Wheelock, M. J. N-Cadherin Promotes Motility in Human Breast Cancer Cells Regardless of Their E-Cadherin Expression. *J. Cell Biol.* **1999**, *147*, 631–644.
- (76) Takeichi, M. Self-Organization of Animal Tissues: Cadherin-Mediated Processes. *Dev. Cell* **2011**, *21*, 24–26.
- (77) Alberts, B.; Johnson, A.; Lewis, J.; Raff, M.; Roberts, K.; Walter, P. *Molecular Biology of the Cell*, 4th ed.; Garland Science, 2002.
- (78) Wadell, H. Volume, Shape, and Roundness of Rock Particles. J. Geol. 1932, 40, 443–451.
- (79) Cruz-Matías, I.; Ayala, D.; Hiller, D.; Gutsch, S.; Zacharias, M.; Estradé, S.; Peiró, F. Sphericity and Roundness Computation for Particles Using the Extreme Vertices Model. *J. Comput. Sci.* **2019**, *30*, 28–40.